ARMY RESEARCH LABORATORY

An Analysis of Atmospheric Aerosol Scattering for Mid-Infrared Systems

by Richard C. Shirkey and Sean G. O'Brien

ARL-TR-3938 September 2006

Approved for public release; distribution is unlimited.

NOTICES

Disclaimers

The findings in this report are not to be construed as an official Department of the Army position unless so designated by other authorized documents.

Citation of manufacturer's or trade names does not constitute an official endorsement or approval of the use thereof.

Destroy this report when it is no longer needed. Do not return it to the originator.

Army Research Laboratory
White Sands Missile Range, NM 88002-5501

ARL-TR-3938 **September 2006**

An Analysis of Atmospheric Aerosol Scattering for Mid-Infrared Systems

Richard C. Shirkey and Sean G. O'Brien
Computational and Information Sciences Directorate

Approved for public release; distribution is unlimited.

REPORT DOCUMENTATION PAGE

Form Approved
OMB No. 0704-0188

Public reporting burden for this collection of information is estimated to average 1 hour per response, including the time for reviewing instructions, searching existing data sources, gathering and maintaining the data needed, and completing and reviewing the collection information. Send comments regarding this burden estimate or any other aspect of this collection of information, including suggestions for reducing the burden, to Department of Defense, Washington Headquarters Services, Directorate for Information Operations and Reports (0704-0188), 1215 Jefferson Davis Highway, Suite 1204, Arlington, VA 22202-4302. Respondents should be aware that notwithstanding any other provision of law, no person shall be subject to any penalty for failing to comply with a collection of information if it does not display a currently valid OMB control number.
PLEASE DO NOT RETURN YOUR FORM TO THE ABOVE ADDRESS.

1. REPORT DATE *(DD-MM-YYYY)*	2. REPORT TYPE	3. DATES COVERED (From - To)
September 2006	Final	Jan 2005 – July 2006

4. TITLE AND SUBTITLE
An Analysis of Atmospheric Aerosol Scattering for Mid-Infrared Systems

5a. CONTRACT NUMBER

5b. GRANT NUMBER

5c. PROGRAM ELEMENT NUMBER

6. AUTHOR(S)
Richard C. Shirkey and Sean G. O'Brien

5d. PROJECT NUMBER

5e. TASK NUMBER

5f. WORK UNIT NUMBER

7. PERFORMING ORGANIZATION NAME(S) AND ADDRESS(ES)
U.S. Army Research Laboratory
Computational and Information Sciences Directorate
Battlefield Environment Division (ATTN: AMSRD-ARL-CI-EE)
White Sands Missile Range, NM 88002-5501

8. PERFORMING ORGANIZATION REPORT NUMBER
ARL-TR-3938

9. SPONSORING/MONITORING AGENCY NAME(S) AND ADDRESS(ES)
U.S. Army Research Laboratory
2800 Powder Mill Road
Adelphi, MD 20783-1145

10. SPONSOR/MONITOR'S ACRONYM(S)

11. SPONSOR/MONITOR'S REPORT NUMBER(S)
ARL-TR-3938

12. DISTRIBUTION/AVAILABILITY STATEMENT
Approved for public release; distribution is unlimited.

13. SUPPLEMENTARY NOTES

14. ABSTRACT
Electro-optical sensors that operate in the mid-infrared region of the electromagnetic spectrum (from 3–5 μm) in the planetary boundary layer can detect atmospheric radiance from a number of source mechanisms, including scattering of direct solar radiation, thermal emission radiance, and secondary scattered thermal radiance from all aerosols and gases. While scattered radiation is of little consequence in the far-infrared region, in the mid-infrared it can reduce a sensor's ability to detect targets by reducing their contrast. In order to determine under what atmospheric conditions scattering in the mid-infrared is significant, we present an analysis of the scattering and emission of some typical aerosols under varying atmospheric conditions. To further delineate whether or not scattering is significant, we present contrast calculations, define a "scattering fraction," and present examples of hypothetical sensor curves for determination of optimal spectral placement in the mid-infrared. In general, we find that for most aerosols and atmospheric conditions, scattering in the mid-infrared cannot be ignored and greatly reduces the contrast available for target detection.

15. SUBJECT TERMS
Mid-infrared, scattering, aerosols, sensor curves

16. SECURITY CLASSIFICATION OF:			17. LIMITATION OF ABSTRACT	18. NUMBER OF PAGES	19a. NAME OF RESPONSIBLE PERSON
a. REPORT	b. ABSTRACT	c. THIS PAGE			Richard C. Shirkey
U	U	U	SAR	48	19b. TELEPHONE NUMBER (*Include area code*) (505) 678-5470

Standard Form 298 (Rev. 8/98)
Prescribed by ANSI Std. Z39.18

Contents

List of Figures **iv**

List of Tables **vi**

Executive Summary **vii**

1. Introduction **1**

2. Study Scenarios and Methods **4**

3. Results **7**

3.1 Maximum Scattering Spectral Radiance 7

3.2 Maximum Emission Spectral Radiance 8

3.3 Contrast—Apparent ΔT 13

3.4 The Scattering Fraction 17

3.4.1 Temperature and Humidity Effects 17

3.4.2 Visibility Effects 21

3.5 Equivalent Blackbody Temperature 25

3.6 Instrument Response Function Effects 26

4. Discussion and Conclusions **32**

References **33**

Acronyms **34**

Distribution List **35**

List of Figures

Figure 1. The various target and atmospheric radiative components. 3

Figure 2. Extinction (solid lines), scattering (dashed lines) and absorption (dot-dash lines) coefficients for the urban (blue), heavy advection fog (magenta) and desert (green) aerosols in the mid-IR band. 6

Figure 3. Radiance components for the fog aerosol at a range of 6 km and a visibility of 5 km in the mid-IR band. The SAW profile was employed. 8

Figure 4. Radiance components for the urban aerosol at a range of 6 km and a visibility of 5 km in the mid-IR band. The MLS profile was employed. 9

Figure 5. Same as figure 4, but smoothed using a 50-point moving average. 9

Figure 6. Smoothed 50-point moving average of the radiance components for the urban aerosol at a range of 6 km and a visibility of 5 km in the mid-IR band. The SAW profile was employed. 10

Figure 7. Smoothed 25-point moving average of the radiance components for the far-IR band. The parameters are the same as figure 5. 11

Figure 8. Smoothed 25-point moving average of the radiance components for the far-IR band. The parameters are the same as figure 6. 11

Figure 9. Smoothed 50-point moving average of the radiance components for the desert aerosol at a range of 6 km and a visibility of 5 km in mid-IR band. The MLS profile was employed. 12

Figure 10. Smoothed 50-point moving average of the radiance components for the desert aerosol at a range of 6 km and a visibility of 5 km in the mid-IR band. The SAW profile was employed. 13

Figures 11–13. Apparent ΔT for the desert aerosol using the three model atmospheres. 14

Figures 14–16. Apparent ΔT for the urban aerosol using the three model atmospheres. 15

Figures 17–19. Apparent ΔT for the fog aerosol using the three model atmospheres. 16

Figures 20–22. The scattering fraction as a function of temperature for the heavy advection fog, wind-dependent desert, and urban aerosol models as a function of the MLS, MLW, and SAW atmospheric profiles at mid-IR wavelengths. 18

Figure 23. Extinction coefficients vs. wavelength for the urban aerosol model for different relative humidities (*3*). 20

Figure 24. Scattering fraction of the urban aerosol at a relative humidity of 91% and 76%. The MLS profile was employed. 21

Figures 25–33. The scattering fraction as a function of visibility for the heavy advection fog, wind-dependant desert, and urban aerosols for the MLS, MLW, and SAW atmospheric profiles at mid-IR wavelengths. 22

Figure 34. The scattering fraction components for the heavy advection fog at 4.0 μm. The MLS atmospheric profile was employed. 24

Figures 35. Equivalent blackbody temperature for the urban and desert aerosols with a visibility of 5 km as a function of range, in mid- and far-IR wavelength bands for the MLS atmospheric profile with an ambient temperature of 21 °C. 25

Figure 36. Equivalent blackbody temperature for the urban and desert aerosols with a visibility of 5 km as a function of range, in mid- and far-IR wavelength bands for the SAW atmospheric profile with an ambient temperature of -16 °C. 26

Figure 37. Apparent target thermal contrast for the desert aerosol employing the MLS atmosphere, with transmission optimized (green) and scattering optimized (black) instrument response functions. 28

Figure 38. Apparent target thermal contrast for the desert aerosol employing the SAW atmosphere, with transmission optimized (green) and scattering optimized (black) instrument response functions. 29

Figure 39. Apparent target thermal contrast for the urban aerosol employing the MLS atmosphere, with transmission optimized (green) and scattering optimized (black) instrument response functions. 29

Figure 40. Apparent target thermal contrast for the urban aerosol employing the SAW atmosphere, with transmission optimized (green) and scattering optimized (black) instrument response functions. 30

List of Tables

Table 1. Component number, as appearing in figure 1, related to the mid-IR atmospheric components in figures 3–10. 4

Table 2. Parameters used in this study. 5

Table 3. Band averaged albedo and average asymmetry values for aerosols used in this study. 6

Table 4. Clear-air transmission from surface level to 100 km along a vertical path using the MLS and MLW atmospheres. 25

Table 5. Apparent target contrast for desert aerosol employing the MLS atmosphere using different optimizations and instrument response functions. 30

Table 6. Apparent target contrast for desert aerosol employing the SAW atmosphere using different optimizations and instrument response functions. 31

Table 7. Apparent target contrast for urban aerosol employing the MLS atmosphere using different optimizations and instrument response functions. 31

Table 8. Apparent target contrast for urban aerosol employing the SAW atmosphere using different optimizations and instrument response functions. 31

Executive Summary

Scattering and absorption by atmospheric aerosols varies greatly depending upon the aerosol chemical composition, the aerosol size distribution, the atmospheric conditions, and the region of the spectrum being examined. In the visible (0.2–0.7 μm) and near-infrared (IR) (0.8–2.0 μm) portions of the spectrum, scattering by atmospheric molecular gases and aerosols is the dominant contributor to atmospheric path radiance. In the far-IR (8–12 μm), thermal emission is the dominant mechanism. However, in the mid-IR spectral region (3–5 μm), scattering of solar radiation by atmospheric aerosols and molecular gases; thermal emission radiance produced by aerosols and molecular gases; and secondary scattered thermal radiance from aerosols and molecular gases all must be considered. The calculation of atmospheric radiance noise for target detection using forward-looking IR (FLIR) devices is considerably simplified by operating in the far-IR band, where only the thermal emission radiance is considered and the scattered radiance can safely be ignored due to atmospheric absorption. However, as technology progresses and sensors are developed that can more efficiently operate in the mid-IR, the significance of scattering effects on atmospheric path radiance, and thus the contrast from which target acquisition is determined, must be assessed. In this report, the environmental conditions in which this assumption may or may not be valid are examined. Since the range of atmospheric parameters is essentially unlimited, we have constrained the parameters for this study to the following: a range of 6 km; midlatitude summer and winter, and subarctic winter model atmospheres (from which the temperatures and humidities were obtained); heavy advection fog, wind-dependent desert, and humidity-dependent urban aerosol models; visibilities of 2, 5, 10, 25, and 50 km; and a value for delta T (or ΔT) of 1.5 K.

For the atmospheric conditions examined, we found that the maximum *scattering* spectral radiance occurred in a foggy, cold, low visibility situation; aerosol scattering of the solar irradiance is the dominant path radiance mechanism from 3.4–4.1 μm; thermal radiance dominates in the virtually opaque 4.1–4.4 μm region; and aerosol-scattered thermal radiance dominates from 4.4–5.0 μm. The 3.0–3.4 μm band is dominated by aerosol-scattered solar irradiance at wavelengths where the atmospheric transmission is highest; where the transmission is relatively low, thermal emission and scattered thermal emission are comparable and dominant.

We also found that the maximum *emission* spectral radiance occurred for the urban, warm, low visibility situation; thermal emission is dominant from 3.0–3.3 μm and from 3.6–5.0 μm. In the 3.3–3.6 μm window region, thermal emission still dominates, but the aerosol-scattered solar irradiance is significant and cannot be ignored for accurate integrated path radiance estimates.

We also calculated the metric currently used in the far-IR for target detection, the difference in apparent temperature between the background and target, commonly refered to as ΔT. ΔT's were calculated in the mid-IR by the current method, that is, considering just the directly transmitted target emission, and second by considering all atmospheric effects, that is, including all scattering and emission effects. Comparing both methods, it can be seen that including atmospheric scattering and atmospheric thermal emission greatly reduced the apparent ΔT in the mid-IR band.

We defined a figure of merit parameter, the "scattering fraction," which highlights the effects of aerosol scattering along any given line of sight. It is comprised of the following radiances: the atmospheric-scattered incident solar plus the scattered atmospheric thermal emission, divided by the atmospheric-scattered incident solar plus the scattered atmospheric thermal emission plus the direct, attenuated (unscattered) thermal radiance. For all of the aerosols, we found that the effect of warmer temperatures could clearly be seen insofar as the scattering fractions were less at all wavelengths, indicative of increased thermal emission. The effects of mid-IR scattering were significant for all three aerosols in all model atmospheres at virtually all wavelengths. There were a few cases, centered about the 3.2 and 4.3 μm wavelengths, where the scattering fraction was relatively low, but these corresponded to regions that also have relatively low mid-IR transmission due to line and continuum absorption. It could also be seen that as the humidity increased, there was a decrease in the scattering fraction, and, as might be expected, aerosols with the highest albedos had the highest scattering fraction. Finally, there is also a progressive movement towards increased scattering fractions for all aerosol types as the visibility decreased.

To provide a real world flavor, hypothetical optimal instrument spectral response functions were constructed. The results showed that a bimodal instrument response function consistently provided higher target contrast than a uniform response function. This was because the strong spectral absorption feature, located between 4.2 μm and 4.4 μm, was excluded in the former case, but not in the latter. This feature essentially allows the sensor to see only the atmospheric emission, thus adding considerable noise to the overall sensed radiance signal. Therefore, any sensor response function that blocks that noise signal would improve performance.

In conclusion, to take advantage of sensing in the mid-IR band, particularly for target acquisition purposes, atmospheric scattering must be taken into account. Sensor performance can be significantly improved in the mid-IR by excluding strong molecular absorption and aerosol scattering wavelength regions through appropriate choices of instrument response functions. Including atmospheric scattering and thermal emission greatly reduces the apparent ΔT, leading to perhaps the most important conclusion, that using the current method of determining ΔT will produce incorrect contrasts and target acquisition ranges at mid-IR wavelengths.

1. Introduction

The field performance of tactical electro-optical (EO) imaging systems used by the Army is sometimes significantly degraded by atmospheric conditions near the surface of the earth. This is especially true in the visible band where scattering from natural aerosols produces "noise" (i.e., path radiance) and signal attenuation. In contrast calculations, sensors operating in the far infrared (IR) (8–12 μm) wavelength band are not normally subject to scattering effects. For these devices, signal attenuation by molecular absorption and thermal emission from atmospheric components are the principal performance hindrances. Devices that operate between these two extremes—in the mid-IR band (3–5 μm)—see an admixture of scattering, absorption, and thermal emission effects. Our purpose in this technical report is to examine atmospheric aerosols and conditions in the mid-IR that could significantly contribute to scattering in that band, thereby contributing to the path radiance, or atmospheric noise, that a mid-IR sensor must contend with. Such noise increases the difficulty in detecting targets by effectively reducing their contrast.

Aerosols can, to some degree, be characterized by their single scattering albedo and asymmetry parameter, which vary with wavelength and aerosol type. At all wavelengths, aerosols generally scatter radiation out of the line of sight (LOS) into various angles. The probability of scattering per particle encounter is given by the single scattering albedo (ϖ_0), which is related to the aerosol volume extinction coefficient κ. κ, which determines the attenuation of the incident radiation, is composed of two parts:

- A scattering coefficient κ_s that describes the radiation scattered out of the LOS without a change in wavelength
- The absorption coefficient κ_a that describes the amount of radiation along the LOS that is converted into other forms of energy or that undergoes a change in wavelength

We can relate the single scattering albedo to κ, and its parts, by the following relation

$$\varpi_0 = \kappa_s/\kappa = \kappa_s / (\kappa_s + \kappa_a). \tag{1}$$

Thus, the albedo ϖ_0 represents the probability that interacting radiation will be scattered rather than absorbed: for pure scattering, $\varpi_0 = 1$, and for total absorption, $\varpi_0 = 0$.

The asymmetry factor, g, is a relative measure of the importance of forward or backward scattering. For isotropic scattering, g is 0; for aerosols that scatter predominantly in the forward direction, as is common at visible wavelengths, g approaches its maximum value of 1. The asymmetry factor also admits to a negative solution, where the aerosol would scatter in the

reverse direction (180°). The asymmetry factor is defined as the average cosine of the scattering angle weighted by the phase function P(θ):

$$g = \langle \cos\theta \rangle = \int_{4\pi} \cos\theta \, P(\theta) \, d\Omega \, / \int_{4\pi} P(\theta) \, d\Omega, \tag{2}$$

where Ω is the solid angle.

The phase function, or angular scattering distribution, gives the directional distribution of radiation scattered by the aerosol under consideration: the phase function is proportional to the probability that incoming radiation is scattered through a scattering angle θ into an element of solid angle dΩ. For incident unpolarized radiation, the phase function is usually normalized as

$$\int_{4\pi} P(\theta) \, d\Omega = 1.0. \tag{3}$$

Scattering of incident solar, atmospheric thermal, and terrain thermal radiation by atmospheric aerosols can make significant contributions to the radiance budget in the mid-IR band (*1*). However, what is not so obvious are the quantitative criteria under which mid-IR scattered radiance is deemed significant relative to the thermal emissive radiance. The combinations of wavelength, range, temperature, cloud cover, aerosol types, visibilities, humidities, source, time of day, and location can easily lead to an exceedingly large number of combinations. Coupling this to various target types and operating conditions leads to an infinite set of overall conditions For this reason, we have limited this study to one target range, two wavelength bands, three model atmospheres (equating to three background temperatures), three aerosol types, five visibilities, and one value for delta T (in this document, we interchangeably use delta T and ΔT); all other parameters were held constant. Using this limited set of environmental and target configurations, we will demonstrate where aerosol scattering may or may not significantly influence the path radiance, or noise signal, and thus attenuation of the target signal. At a later point, we apply these results to better define studies of aerosol scattering effects for more specific sensor response functions and atmospheric conditions.

The radiative transfer (RT) model used to determine the various radiative components is the Moderate Resolution Transmission (MODTRAN) model (*2*). The recent versions of this package include a discrete-ordinates model for RT calculations in a layered atmosphere as well as a database of aerosol scattering properties that has been in existence for many years. MODTRAN includes a solar/lunar top-of-atmosphere irradiance model and treats multiple scattering and thermal emission effects at a moderate spectral resolution of 1 cm^{-1}.

The atmospheric components of the spectral radiance are detailed in figure 1.

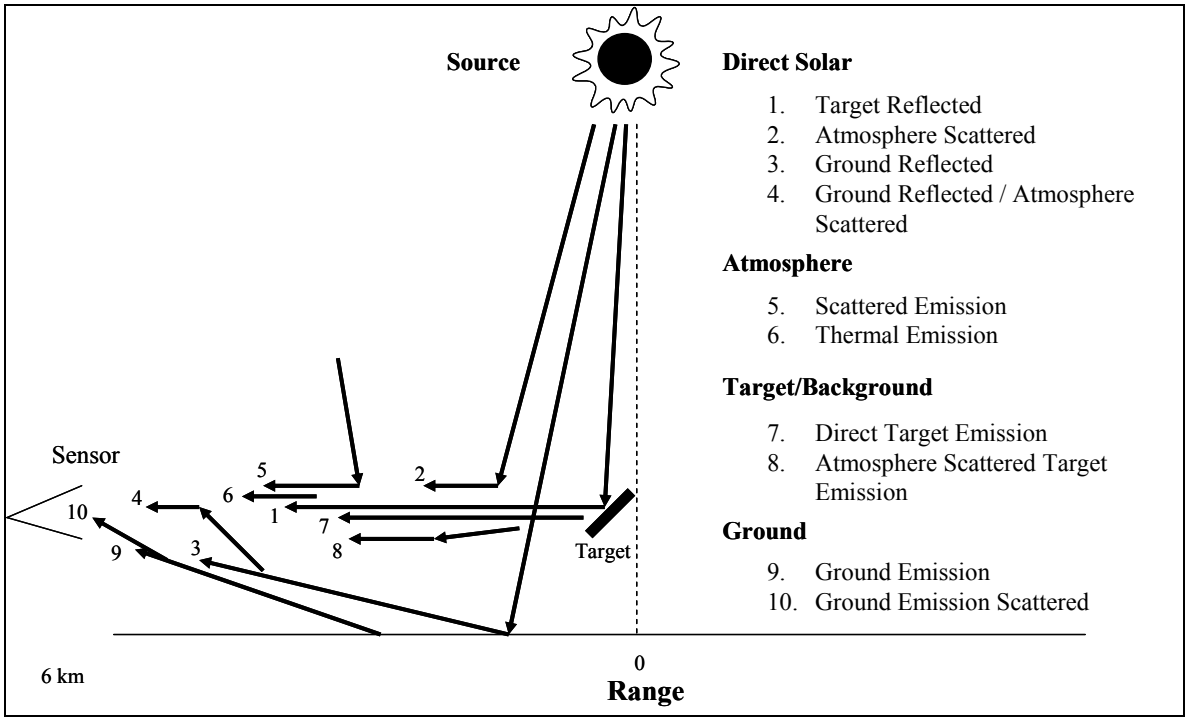

Figure 1. The various target and atmospheric radiative components.

While there will always be situations where all of these radiative components must be considered or one of them may be dominant, for this study, many of the components depicted in figure 1 were not considered. To maximize target emission and reduce target reflection, we chose to set the target albedo to zero, leading to component 1 being zero. Ground emission can, in some instances, particularly when the sensor is looking downward or the ground temperature is high, be significant. However, since our primary purpose here was to examine atmospheric scattering effects, we chose to ignore ground emission and its subsequent scattering by the atmosphere. The latter effect is relatively small in relation to the atmospheric scattering of the other components. MODTRAN options allow setting the ground emission and the surface bidirectional reflectance distribution function to zero, which was done. This, in effect, sets components 3, 4, 9, and 10 to zero. The ambient surface temperature of each model atmosphere was used as the background temperature. A ΔT value of 1.5 K provided the foreground temperature and was used as the target blackbody temperature, which allowed for subsequent contrast determinations. The apparent target radiance, calculated by combining the appropriate non-zero atmospheric components (2, 5, 6, and 7) is presented in figures 3–10. However, the non-zero background radiance, comprised of components 2, 5, and 6, is not plotted and does not appear in those figures. Table 1 relates the non-zero components in figure 1 to figures 3–10.

Table 1. Component number, as appearing in figure 1, related to the mid-IR atmospheric components in figures 3–10.

Component Number	Atmospheric Component
2	Solar Scattered
5	Atmospheric Scattered Emission
6	Atmospheric Emission
7	Direct Transmitted Target Emission

The graphs also present the transmission through atmospheric gases and the selected aerosol over the path length considered for mid-IR wavelengths.

Finally, it should be noted by the reader that our "sensor" does not have a field of view (FOV). Rather, we are concerned here with radiances at the observer's position, and not with irradiances or fluxes that ordinarily would be presented for a sensor with an FOV.

2. Study Scenarios and Methods

Since we are concerned with RT results within the Army domain of operations, our results have been for a near-surface (10 m height), horizontal LOS path (6 km) with varying visibilities. To represent significantly different atmospheric profiles, three MODTRAN model atmospheres—midlatitude summer (MLS), midlatitude winter (MLW) and subarctic winter (SAW)—were employed to represent the different absolute humidities and molecular and temperature profiles that strongly affect absorption and background thermal emission, respectively. All atmospheric profiles represent clear (cloudless) conditions. Overcast conditions would be expected to reduce both the ambient solar irradiance and thermal emission in this band, so the relative importance of scattered radiance to thermal radiance would not, at first glance, be greatly modified. Overcast conditions were, therefore, not pursued. Although the solar incidence angle will affect the amount of irradiance received at ground level, to more easily see scattering and emission effects, we have opted to maximize the solar irradiance. Thus, the time of day was set at 1200 local time. Three aerosol models were chosen that had differing characteristics. They were a humidity-dependent urban aerosol (*3*), a heavy advection fog aerosol (*3*), and a humidity independent, wind-dependent desert aerosol model (*4*, *5*) at a wind speed of 10 m/s. To maximize target emission and minimize target scattering, the target's albedo was set to zero. Table 2 presents the surface level temperature and humidity properties of the three model atmospheres along with the parameter space used in this study.

Table 2. Parameters used in this study.

Wavelength Bands (µm)	3–5, 8–12		
Visibilities (km)	2, 5, 10, 25, 50		
Aerosol Types	Humidity-dependent urban Wind-dependent desert Heavy advection fog		
Target/Observer Height (m)	10		
Range (km)	6		
Path Type	Horizontal		
Model Atmospheres	**Surface Ambient Temperature (°C)**	**Surface Relative Humidity (%)**	**Surface Absolute Humidity (g/m^3)**
Midlatitude Summer	21.04	76.17	14.03
Midlatitude Winter	-0.96	77.07	3.51
Subarctic Winter	-15.60	80.46	1.21
Illumination Source	Sun		
Time of Day	1200		
Location	N/A		
Albedo of Earth	N/A[a]		
Target Albedo	Zero		
Delta T (K)	1.5		
Cloud Cover	None		

[a]See discussion in section 1.

The aerosols chosen for this investigation were selected with an eye toward contrasting significant differences in their optical properties as represented by their single scattering albedo and asymmetry parameter (*4*). Table 3 compares the optical properties for these aerosols at the wavelength bands of 3–5 µm and 8–12 µm. In the mid-IR, the urban aerosol (urban), which is the only humidity-dependent aerosol used in this study, has the lowest single scattering albedo and asymmetry parameter, whereas the wind-dependent desert aerosol (desert) has the highest single scattering albedo and an asymmetry parameter factor somewhat higher than the urban model. In the 3–5 µm band, the higher albedo value for the desert aerosol is indicative of stronger scattering characteristics and lower absorption relative to the other aerosols. This characteristic is carried over in the 8–12 µm band, although here the difference in extinction coefficient is primarily due to absorption, since aerosol scattering is minimal in this band. The single scattering albedo of the heavy advection fog aerosol (fog) is intermediate to the desert and urban aerosol types; however it has the highest asymmetry parameter of the three aerosols, an indication of its relatively large particle size and stronger forward scattering portion of its phase function. The heavy advection fog is characteristic of an aerosol with particle sizes significantly larger than wavelengths in the visible and mid-IR bands. As a consequence, the extinction versus wavelength curve of this aerosol is nearly neutral from the visible band into the mid-IR,

so that low meteorological visibilities translate into much higher mid-IR extinction coefficients than for the other aerosols examined here. Additional understanding of the radiative effects that are contributed by the aerosol can be gleaned by examining their extinction, scattering, and absorption coefficients, presented in figure 2 (note that this figure is plotted on a log-log scale). As mentioned above, the most notable difference among the three aerosols is the almost total lack of absorption by the desert aerosol.

Table 3. Band averaged albedo and average asymmetry values for aerosols used in this study.

Model	Albedo		Asymmetry	
	(3–5 µm)	(8–12 µm)	(3–5 µm)	(8–12 µm)
Urban (80% RH)	0.550	0.381	0.743	0.771
Desert (ws = 10 m/s)	0.915	0.676	0.770	0.696
Heavy advection fog	0.689	0.569	0.898	0.931

NOTE: ws = wind speed and RH = relative humidity.

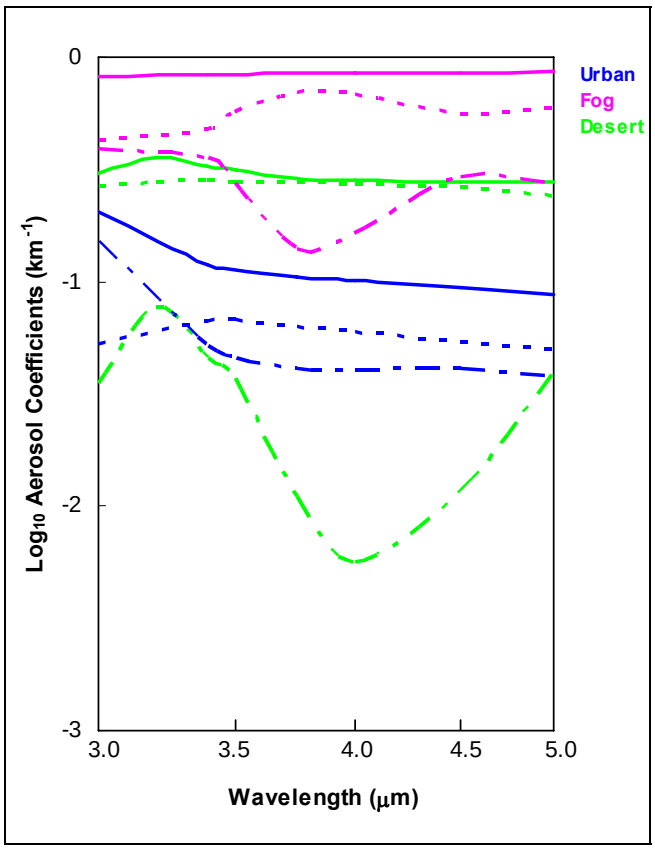

Figure 2. Extinction (solid lines), scattering (dashed lines) and absorption (dot-dash lines) coefficients for the urban (blue), heavy advection fog (magenta) and desert (green) aerosols in the mid-IR band.

NOTE: The extinctions have been normalized to a visibility of 5 km at 0.55 µm and the wavelength is plotted on a $\log_{10}$ scale.

3. Results

In order to know whether or not scattering in the mid-IR is relevant, it is necessary to determine under what conditions scattering predominates and under what conditions emission predominates. Sections 3.1–3.3 separately examine these two competing mechanisms, under which atmospheric conditions they become dominant, and how they influence target contrast. Section 3.4 discusses a metric, the scattering fraction that highlights the effects of aerosol scattering. Other effects, such as humidity and visibility, etc., on scattering and emission in the mid-IR are examined, and a discussion on optimal instrument response function is presented.

3.1 Maximum Scattering Spectral Radiance

Scattering of direct solar irradiance and ambient thermal radiance by the turbid atmosphere are near maximum levels when the aerosol particle size distribution is appreciable at large particle radii relative to the wavelength, the aerosol number density is high, and thermal emission from molecular sources is low. In our selection of model atmospheres, aerosols, and meteorological visibilities, this situation is best matched by the dry, cold SAW atmosphere coupled with the fog aerosol. Figure 3 shows the full band results for this scenario (the right-hand scale represents the transmission curve). The overall atmospheric transmission is quite low due to the 5-km visibility over the 6-km path length. The semi-flat envelope of the transmission curve, with the exception of the CO_2 absorption notch centered around 4.3 μm, is due to the fact that the fog aerosol extinction varies only slowly with wavelength (*3*) (cf., figure 2). Thus, unlike many other atmospheric background aerosols (*3*), a low visibility in the visual band also translates to low visibility in the mid-IR for the fog aerosol. Also note that in all but the 4.1–4.4 μm region of the 3–5 μm band (where a strong CO_2 vibrational absorption feature blots out transmission), some form of scattering dominates. Below 4.1 μm, much of the path radiance is due to scattering of the solar irradiance by the fog aerosol, with the exception of narrow regions below 3.4 μm, where line absorption features are numerous due to another prominent CO_2 absorption band. Thus, for this foggy, cold, low visibility situation, aerosol scattering of the solar irradiance is the dominant path radiance mechanism from 3.4–4.1 μm; thermal radiance dominates in the virtually opaque 4.1–4.4 μm region; and aerosol-scattered thermal radiance dominates from 4.4–5.0 μm. The 3.0–3.4 μm band is dominated by aerosol-scattered solar irradiance at wavelengths where the atmospheric transmission is highest; where the transmission is relatively low, thermal emission and scattered thermal emission are comparable and dominant.

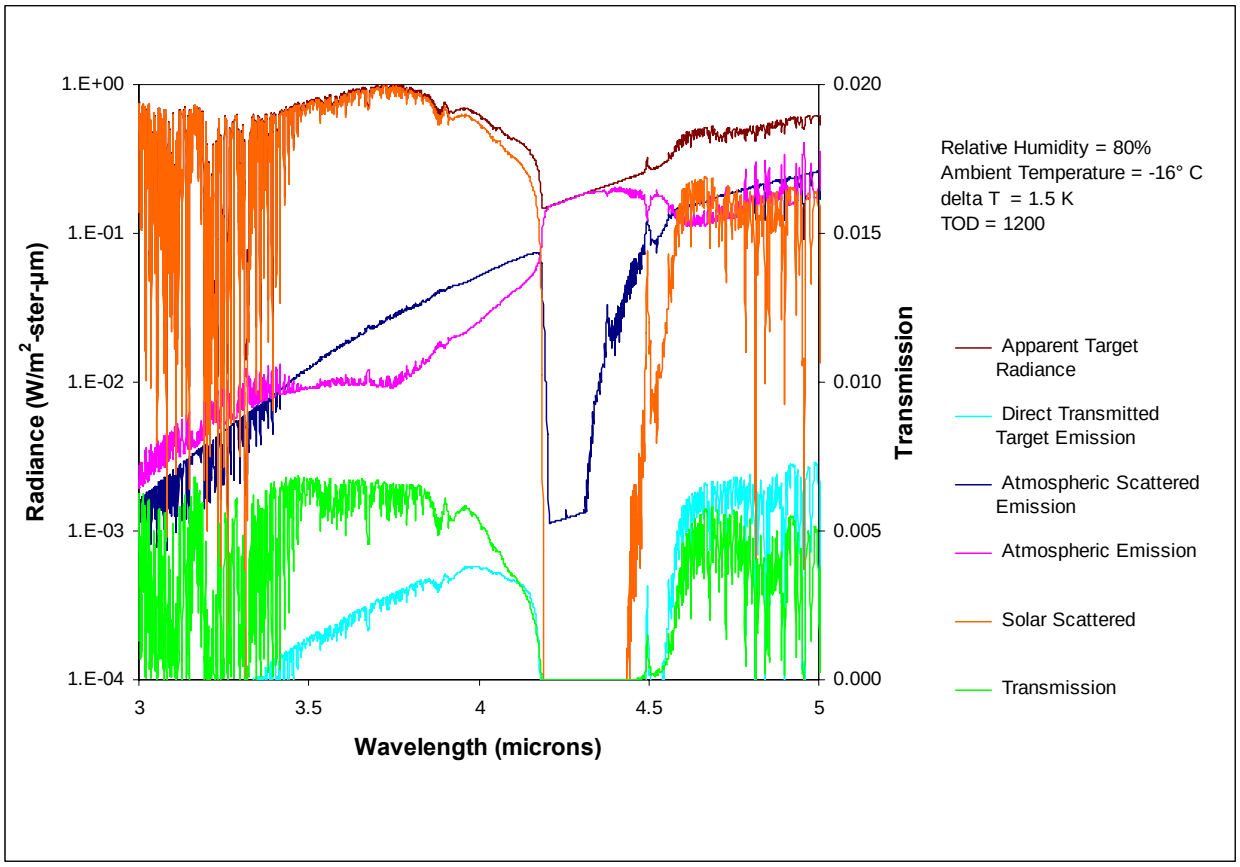

Figure 3. Radiance components for the fog aerosol at a range of 6 km and a visibility of 5 km in the mid-IR band. The SAW profile was employed.

NOTE: TOD = time of day.

3.2 Maximum Emission Spectral Radiance

The environmental scenario in the mid-IR where thermal emission effects can be expected to be at their maximum is where the atmosphere is warm (maximizing ambient temperature) and the background aerosols have a relatively low albedo (maximizing absorption effects). For this case, the urban aerosol in a MLS atmosphere (ambient temperature of 21 °C) at a range of 6 km was used. Figure 4 displays the resulting spectral radiance components and transmission for $\Delta T = 1.5°$ in complete detail; figure 5 (and all subsequent graphs of this type) present the same data, but, for clarity, have been smoothed using a 50-point moving average. As seen from figure 4 or 5, the thermal emission is dominant from 3.0–3.3 µm and from 3.6–5.0 µm. In the 3.3–3.6 µm window region, thermal emission still dominates, but the aerosol-scattered solar irradiance is significant and cannot be ignored for accurate integrated path radiance estimates. Note that, in these figures, the transmission curve corresponds to the right-hand scale; all other radiative curves use the left-hand scale.

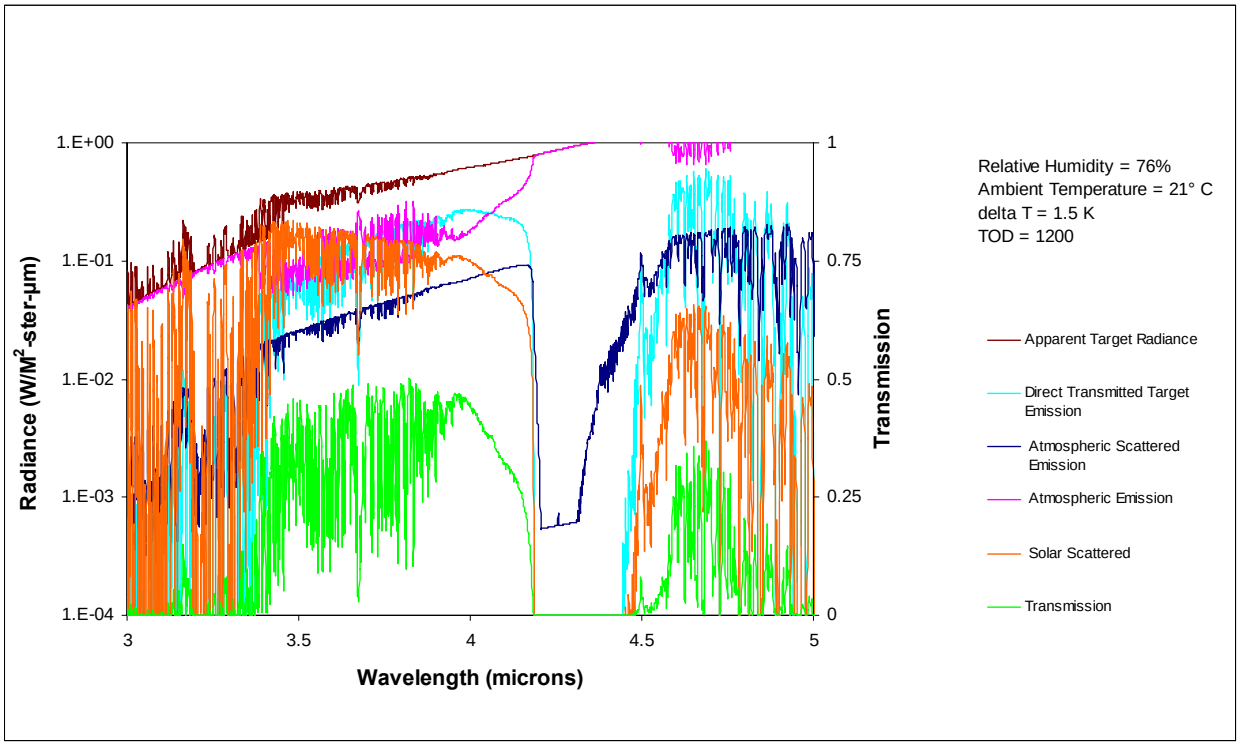

Figure 4. Radiance components for the urban aerosol at a range of 6 km and a visibility of 5 km in the mid-IR band. The MLS profile was employed.

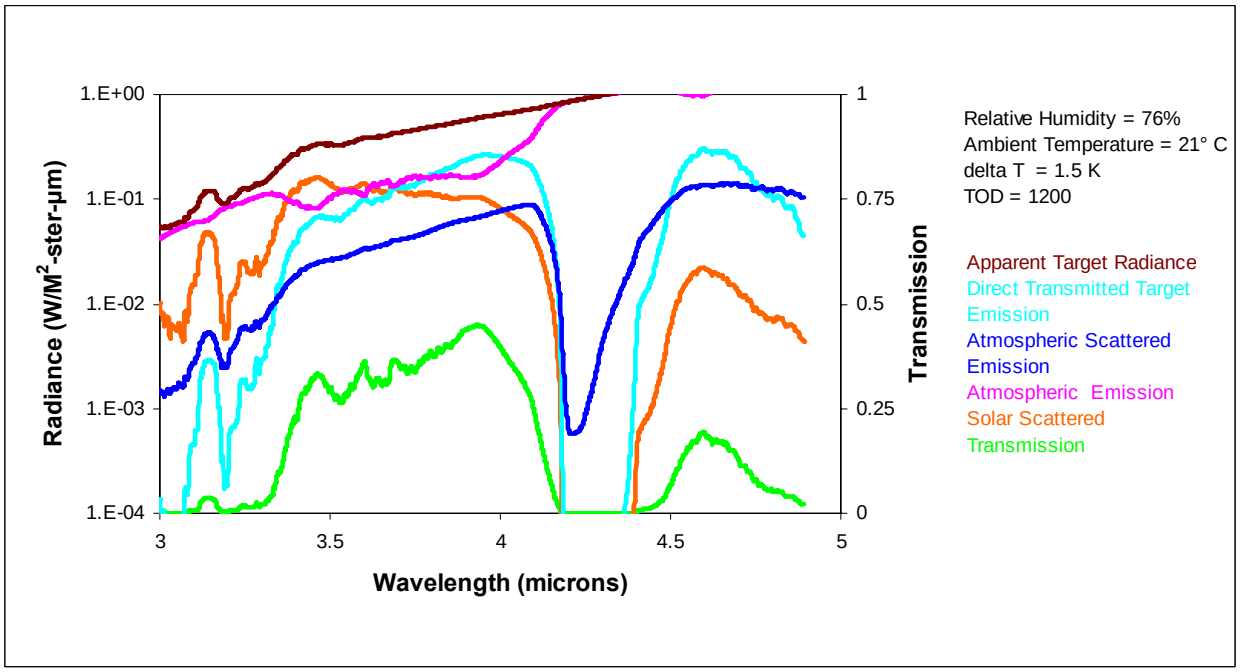

Figure 5. Same as figure 4, but smoothed using a 50-point moving average.

For comparison purposes, figure 6 presents the same scenario as figures 4 or 5, but using the SAW atmosphere (ambient temperature of -16 °C). As expected, the most notable changes in figure 5 are the decrease in the thermal radiance components: shortward of 4.2 µm, scattering is now the dominant process.

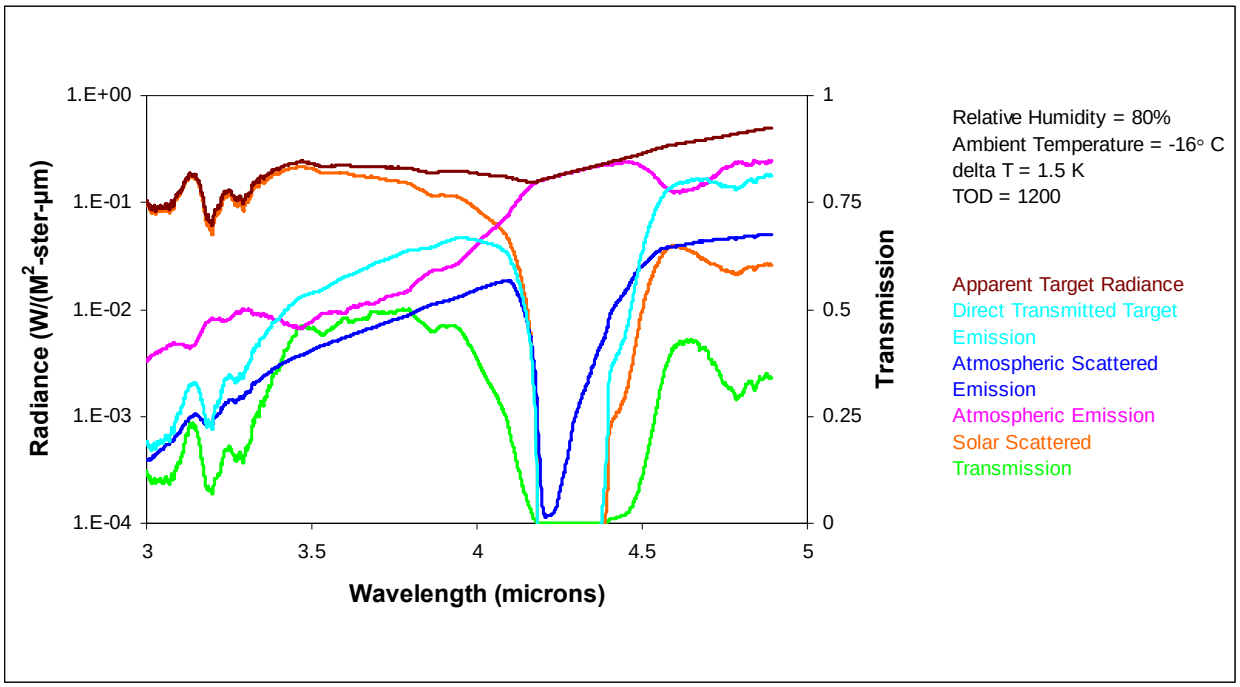

Figure 6. Smoothed 50-point moving average of the radiance components for the urban aerosol at a range of 6 km and a visibility of 5 km in the mid-IR band. The SAW profile was employed.

We also present the equivalent figures for the far-IR band: figure 7 corresponds to figure 5 (urban aerosol, ambient T = 21 °C), and figure 8 corresponds to figure 6 (urban aerosol, ambient T = -16 °C). As may easily be seen, thermal emission is the dominant process with scattering playing an insignificant role for the far-IR.

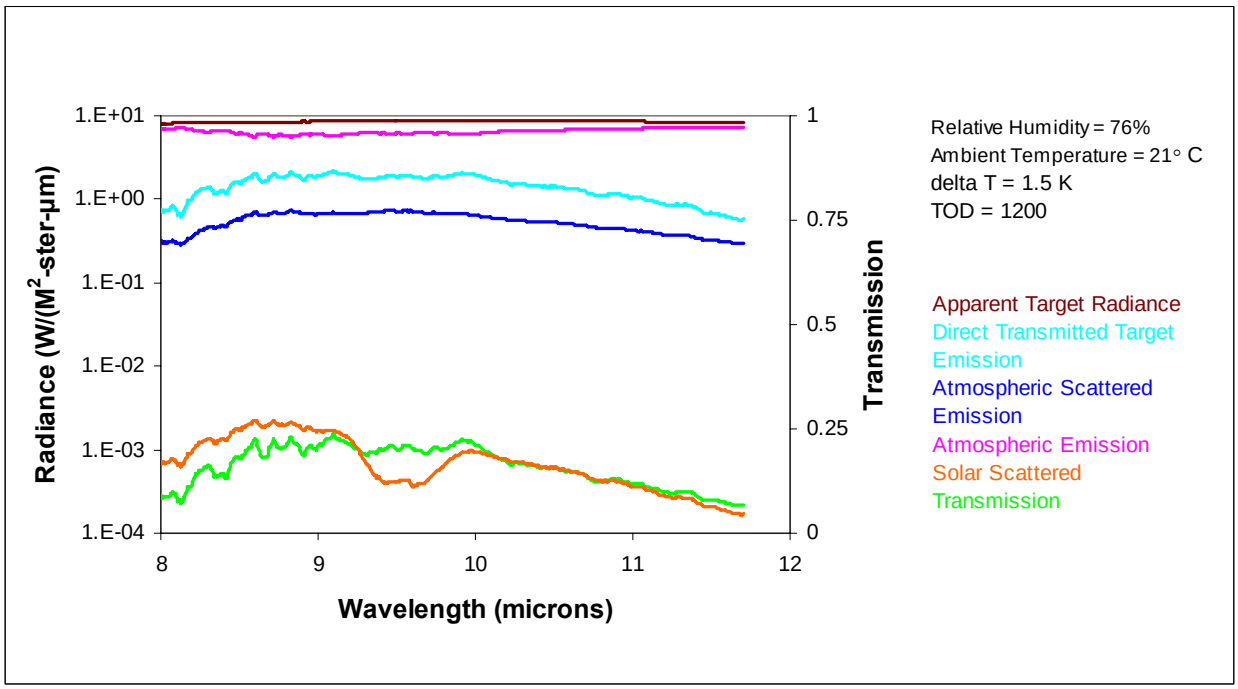

Figure 7. Smoothed 25-point moving average of the radiance components for the far-IR band. The parameters are the same as figure 5.

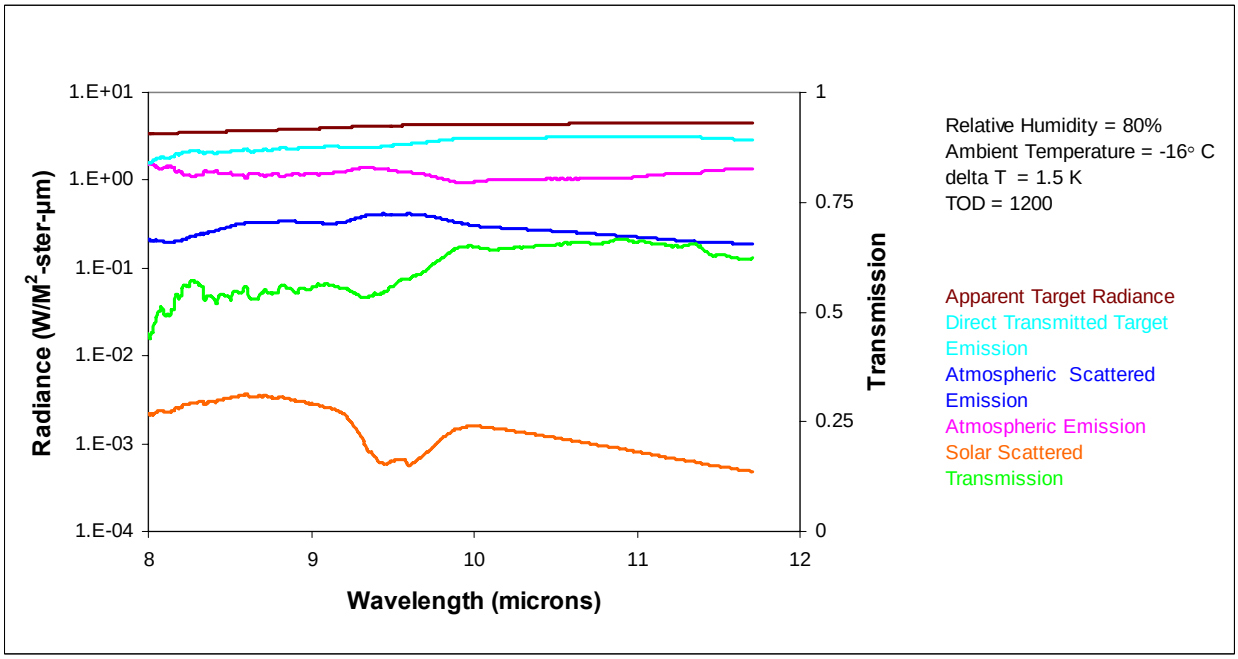

Figure 8. Smoothed 25-point moving average of the radiance components for the far-IR band. The parameters are the same as figure 6.

As a closing inquiry for this section, we examine a case where we have varied only the aerosol type. Contrasting the results of figure 9 (desert) with figure 5 (urban), it may be seen that the scattering is more prominent and the thermal path radiance due to atmospheric emission is reduced. These changes are due primarily to the higher albedo of the desert aerosol. Since a higher albedo implies a higher scattering coefficient and, thus, a lower absorption coefficient (cf., equation 1), these results are in agreement with the scattering and absorption coefficients presented in figure 2 where the desert aerosol consistently has a higher scattering coefficient and lower absorption coefficient relative to the urban aerosol. Comparing the lower background temperatures of -16°C for the urban and desert aerosols (figures 6 and 10, respectively), we again find that for the desert aerosol, the scattering is larger and the path radiance is lower, but the effects are less notable due to the lower ambient temperature and thus the reduced thermal emission.

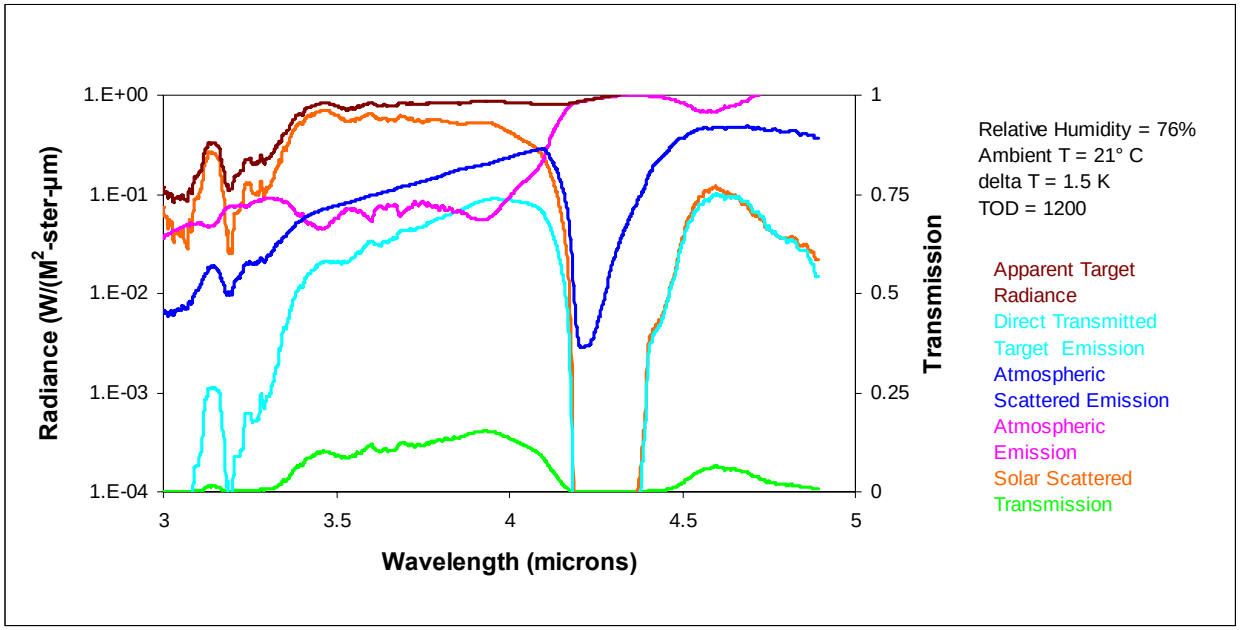

Figure 9. Smoothed 50-point moving average of the radiance components for the desert aerosol at a range of 6 km and a visibility of 5 km in mid-IR band. The MLS profile was employed.

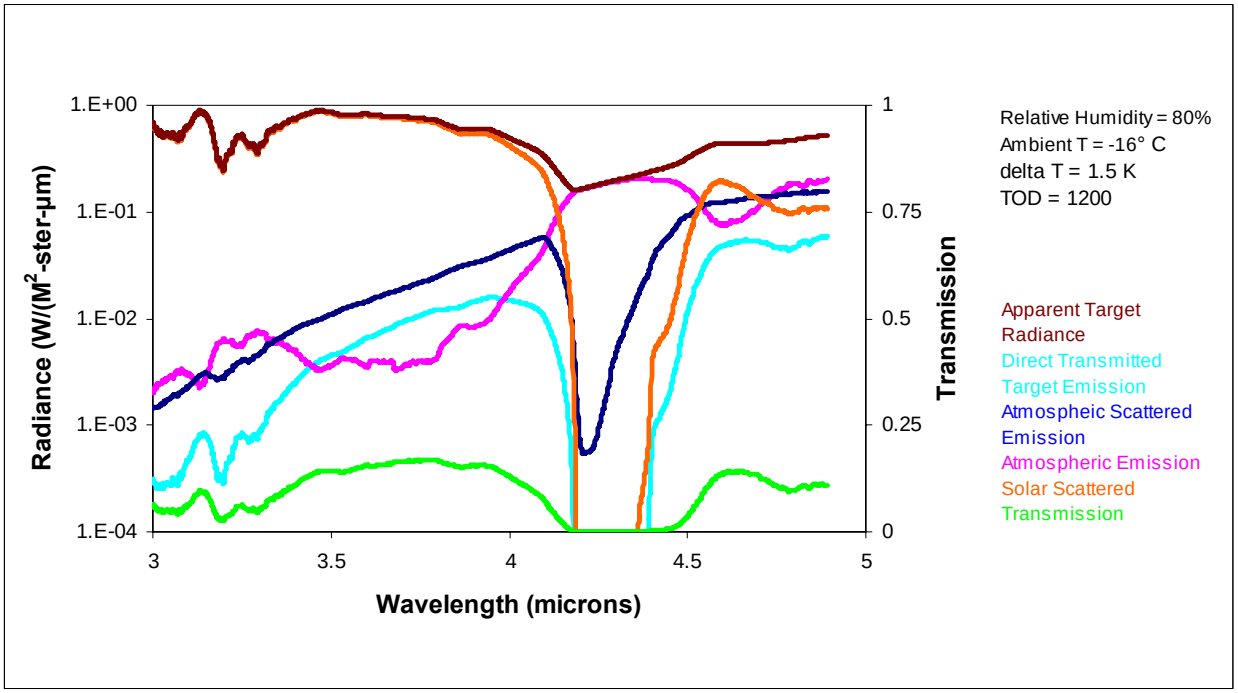

Figure 10. Smoothed 50-point moving average of the radiance components for the desert aerosol at a range of 6 km and a visibility of 5 km in the mid-IR band. The SAW profile was employed.

3.3 Contrast—Apparent ΔT

Since ΔT is determined by the subtracting the foreground (target) temperature (T_t) from the background temperature (T_b), we assigned a value to ΔT, used the surface layer temperature of the employed model atmosphere as T_b and, thus, set $T_t = T_b + \Delta T$. In the figures 11–19, there are two "apparent" ΔT's. The upper ΔT, in magenta, was calculated via the method currently in practice in the far-IR band, (i.e., using just the direct transmitted target emission). The second curve, in blue, uses all atmospheric effects available for the horizontal path (i.e., the apparent target radiance). Note that both of these quantities, the direct transmitted target emission and the apparent target radiance, are shown in figures 3–10. Figures 11–13 show the apparent ΔT's corresponding to the desert aerosol for each of the three model atmospheres in the mid-IR. Figures 14–16 and 17–19 show the same information for the urban and fog aerosols, respectively. Note that for the fog model, the ΔT including all scattering effects is barely visible on all three plots. From these figures, it is immediately seen that including atmospheric scattering and thermal emission greatly reduces the apparent ΔT in the mid-IR band for all three aerosols. Thus, under atmospheric conditions where scattering in the mid-IR is present, using the current method of determining ΔT will be in error.

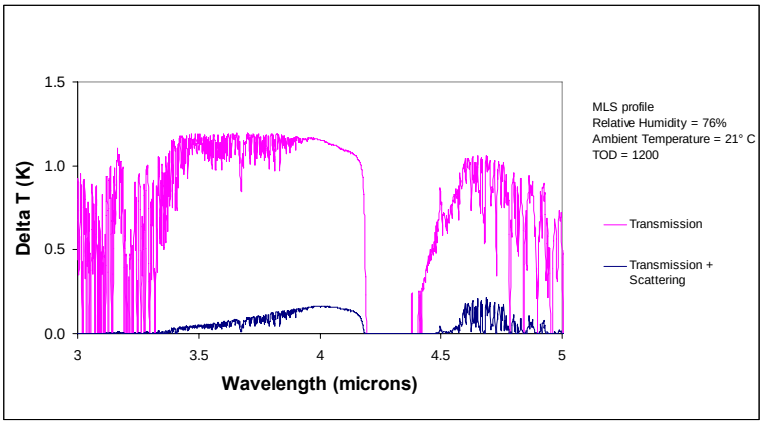

Figure 11.

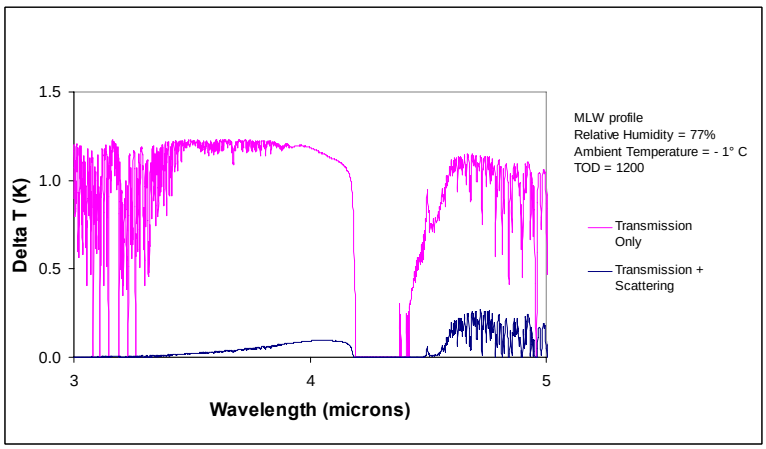

Figure 12.

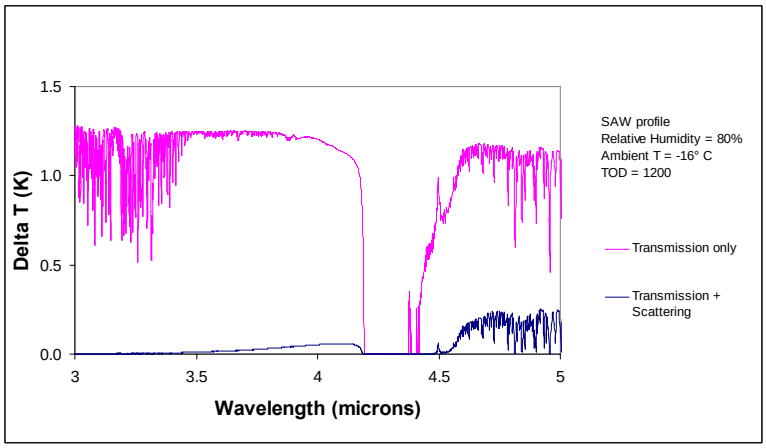

Figure 13.

Figures 11–13. Apparent ΔT for the desert aerosol using the three model atmospheres.

NOTE: The magenta line is transmission only; the blue line includes all scattering effects. ΔT was 1.5 K.

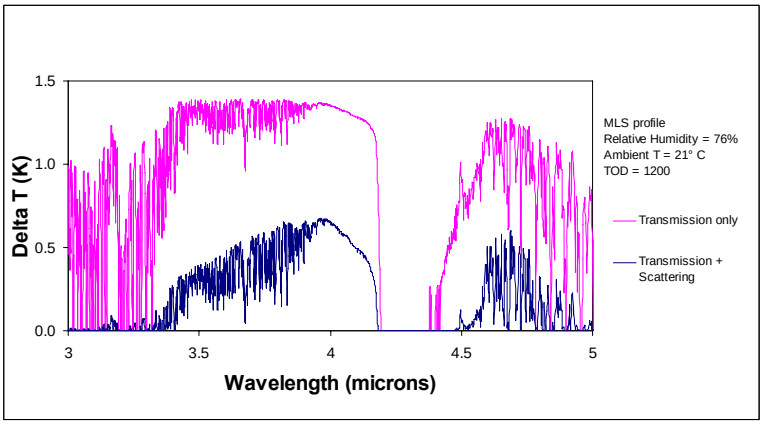

Figure 14.

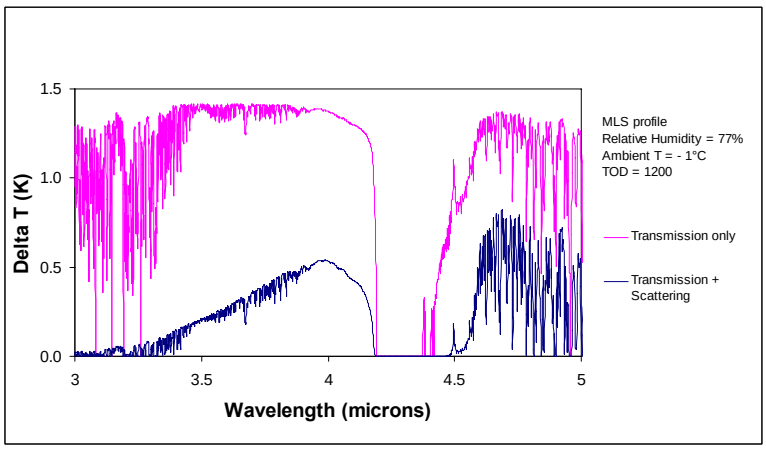

Figure 15.

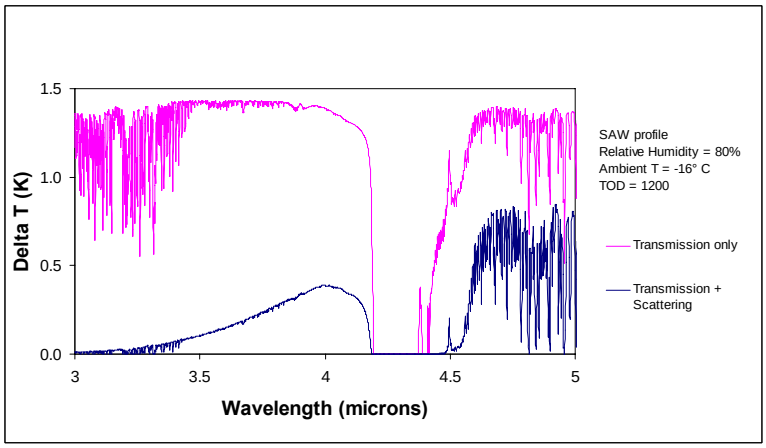

Figure 16.

Figures 14–16. Apparent ΔT for the urban aerosol using the three model atmospheres.

NOTE: The magenta line is transmission only; the blue line includes all scattering effects. ΔT was 1.5 K.

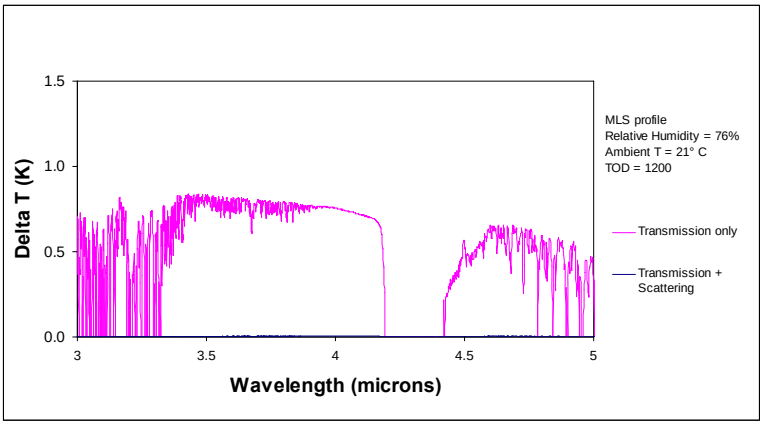

Figure 17.

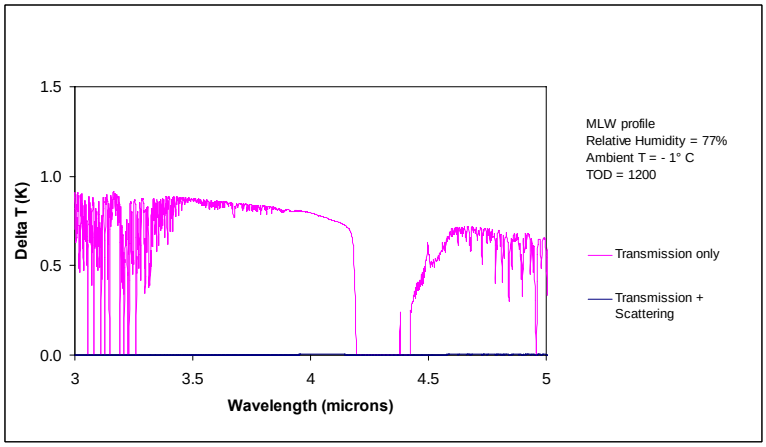

Figure 18.

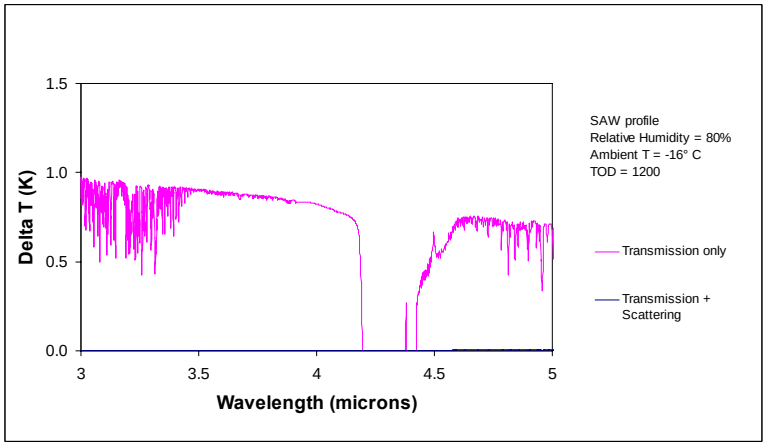

Figure 19.

Figures 17–19. Apparent ΔT for the fog aerosol using the three model atmospheres.

NOTE: The magenta line is transmission only; the blue line includes all scattering effects. ΔT was 1.5 K. Note that the transmission is barely visible, if at all.

3.4 The Scattering Fraction

Departing from the interpretation of radiance values, path transmissions, and ΔT's, we define a figure of merit parameter that highlights the effects of aerosol scattering along any given LOS. We define a "scattering fraction" φ such that

$$\varphi = \frac{L_{SS} + L_{ASE}}{L_{SS} + L_{ATE} + L_{ASE}} = \frac{L_{SS} + L_{ASE}}{L_T}, \tag{4}$$

where L_{SS} *(Solar Scattered)* is the atmospheric-scattered incident solar radiance, component #2 in figure 1; L_{ASE} *(Atmospheric Scattered Emission)* is the scattered atmospheric thermal emission radiance, component #5 in figure 1; L_{ATE} *(Atmospheric Thermal Emission)* is the direct, attenuated (unscattered) thermal radiance, component #6 in figure 1; and L_T is the total of these radiance components. Because scattering in the far-IR is negligible, the scattering fraction in that band would be a relatively straight line as a function of wavelength, with a near-zero amplitude. Thus, we will consider only the mid-IR impacts here where the degree of deviation of φ from zero indicates the degree of significance of scattering effects. Since scattering in the mid-IR band depends mainly on the aerosol characteristics and the amount of the aerosol present along any given LOS, the scattering fraction is nearly invariant with range, but will vary significantly with visibility. As an arbitrary decision criterion, we might assert that the aerosol scattering mechanism is important when the scattering fraction exceeds 10%. For use in the following discussion, we note a few general characteristics of the components of equation 4. Looking at each component, while holding the other two constant, leads to the following effects on φ:

- a decrease when L_{ASE} decreases
- an increase when L_{TE} decreases
- an increase when L_{SS} decreases

Bearing this in mind, we now compare the various scattering effects due to different model atmospheres (i.e., surface temperatures and humidities) and visibilities for the three aerosol models.

3.4.1 Temperature and Humidity Effects

Examining the scattering fraction as a function of model atmosphere for the three aerosols, figures 20–22, it is apparent that the effects of mid-IR scattering are significant for all aerosols at virtually all wavelengths, with the exception of the CO_2 absorption band centered at approximately 4.3 μm.

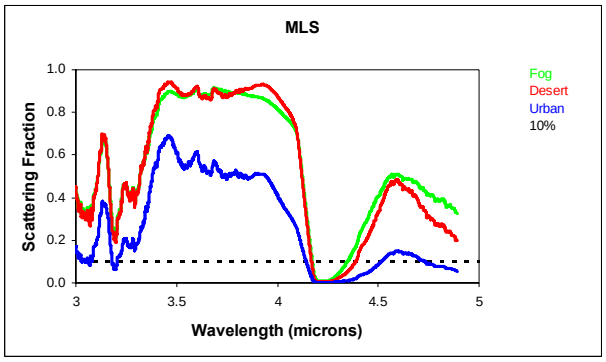

Figure 20.

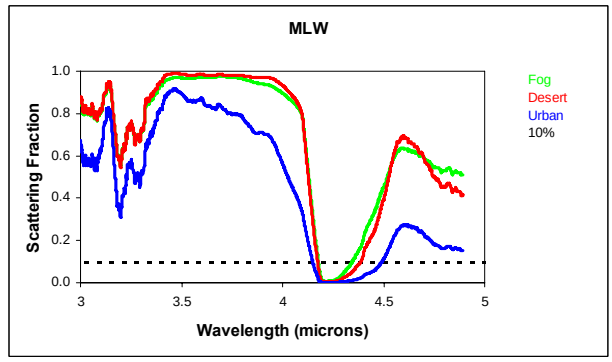

Figure 21.

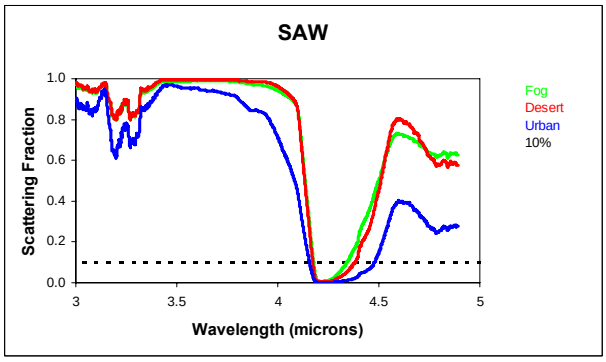

Figure 22.

Figures 20–22. The scattering fraction as a function of temperature for the heavy advection fog, wind-dependent desert, and urban aerosol models as a function of the MLS, MLW, and SAW atmospheric profiles at mid-IR wavelengths.

NOTE: The range is 6 km at a visibility of 5 km.

The MLS atmosphere is the warmest and most humid of the three model atmospheres. The effect of its warmer temperature can clearly be seen insofar as the scattering fraction of the MLS atmosphere is less at all wavelengths, indicative of increased thermal emission, compared to the cooler MLW and cold SAW atmospheres, where the background temperatures are lower. Thus, as we progress from MLS → MLW → SAW and the temperature decreases, the scattering fraction will increase for each aerosol type. It is apparent that the effects of mid-IR scattering are significant for all three aerosols in the selected model atmospheres at virtually all wavelengths. There are a few cases centered about 3.2 and 4.3 μm wavelengths, where the scattering fraction is relatively low, but these correspond to regions that also have relatively low mid-IR transmission due to line and continuum absorption. The decrease in thermal emission may also be seen by comparing figures 5 and 6 (urban aerosol, MLS and SAW, respectively) or figures 9 and 10 (desert aerosol, MLS and SAW, respectively).

We also see from figures 20–22 that the aerosol with the highest albedo, the desert aerosol, has the highest scattering fraction, closely followed by the fog aerosol; the urban aerosol, which has the lowest albedo, also had the lowest scattering fraction. This can also be viewed in terms of the components that make up the albedo. A high albedo implies a high scattering coefficient; a low albedo implies a high absorption coefficient, and it is a well-known fact that good absorbers are good emitters. Thus, the urban aerosol's lower scattering fraction is in accordance with the discussion of path thermal emission effects on scattering fraction above: lower albedo implies higher emission and lower scattering fraction.

For those aerosols that have an extinction efficiency dependence upon humidity, such as the urban aerosol, the surface layer humidity for each of the model atmospheres should be noted. As the extinction coefficient increases, by inference (see equation 1), so does the absorption coefficient and, thus, the emission efficiency of the aerosol. Since the extinction coefficient of the urban aerosol increases with humidity (see figure 23), we expect the emission to also increase with humidity, with a resultant decrease in φ as we progress from SAW → MLW → MLS. While this can be inferred from figures 20–22, the calculations that were used to construct these figures also have considerably different surface temperatures. To more clearly show this effect, we have performed additional calculations using the humidity-dependent urban aerosol at 91% relative humidity, since the fog and desert aerosols do not have this dependence. As expected, and can be seen in figure 24, there is a definite change in the scattering fraction with humidity. As the humidity increases, in general, so will the atmospheric thermal emission resulting in a decrease in the scattering fraction, in accordance with the above discussion.

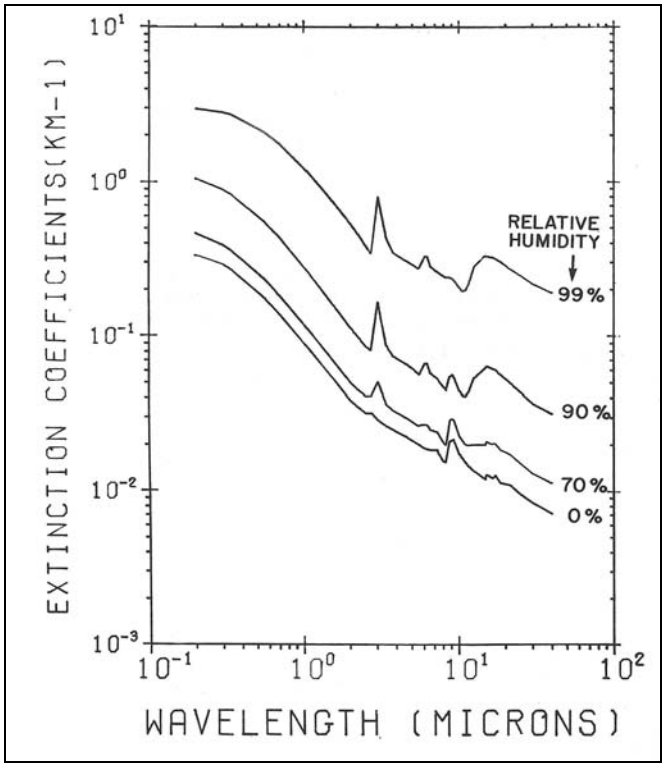

Figure 23. Extinction coefficients vs. wavelength for the urban aerosol model for different relative humidities (*3*).

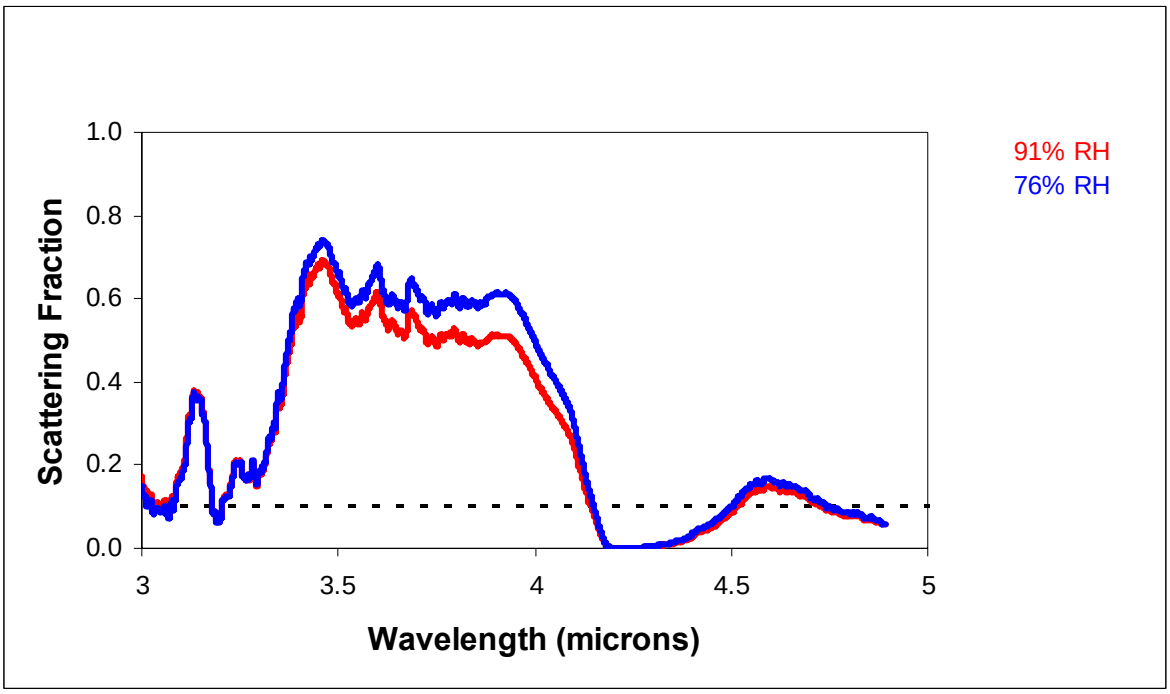

Figure 24. Scattering fraction of the urban aerosol at a relative humidity of 91% and 76%. The MLS profile was employed.

NOTE: The range is 6 km at a visibility of 5 km.

In figures 20–22, the scattering fraction for the three aerosols was examined as a function background temperature and, in figure 24, of humidity. Since changes in aerosol densities are directly related to changes in visibility, it is instructive to examine the changes in the importance of scattering effects due to changes in visibility. Section 3.4.2 examines such changes.

3.4.2 Visibility Effects

Figures 25–33 present changes in the scattering fraction as a function of visibility for the three aerosols using the three model atmospheres. It is easily seen that visibility is also a significant factor when considering relative scattering effects.

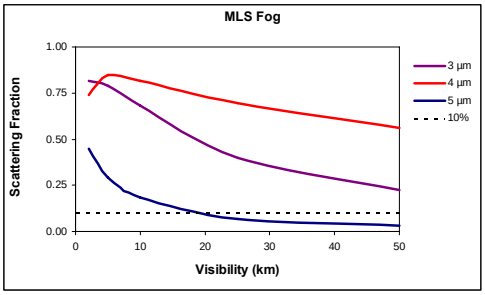

Figure 25.

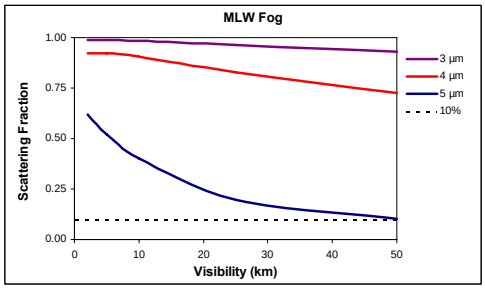

Figure 26.

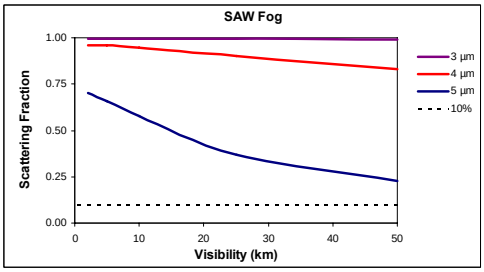

Figure 27.

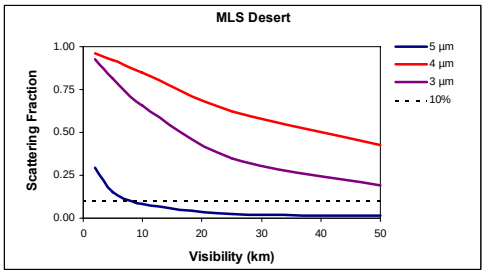

Figure 28.

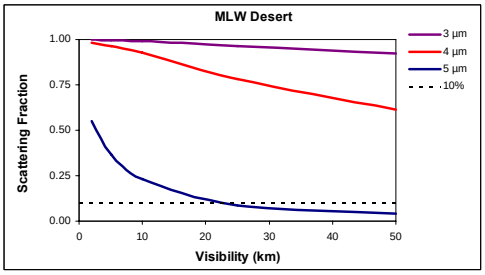

Figure 29.

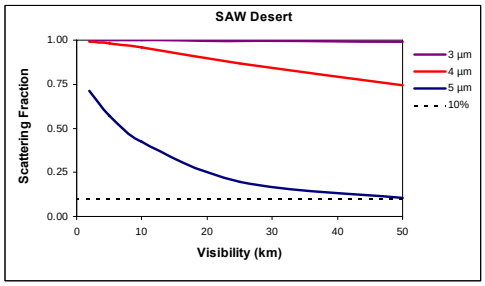

Figure 30.

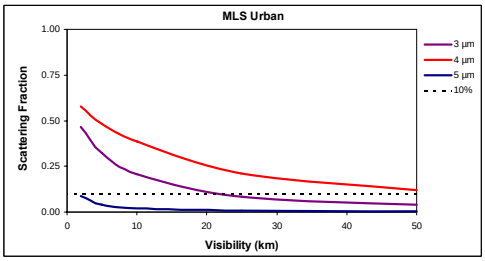

Figure 31.

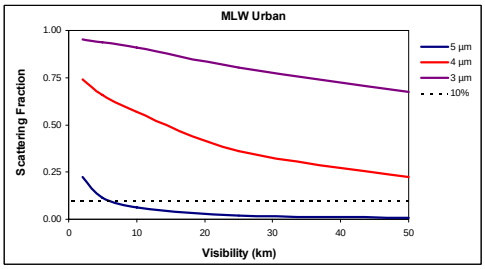

Figure 32.

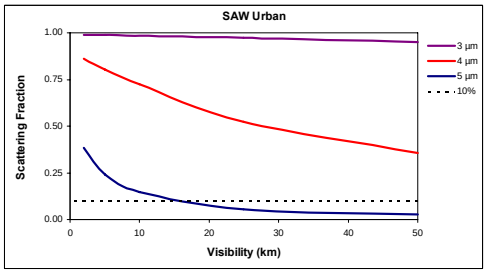

Figure 33.

Figures 25–33. The scattering fraction as a function of visibility for the heavy advection fog, wind-dependant desert, and urban aerosols for the MLS, MLW, and SAW atmospheric profiles at mid-IR wavelengths.

NOTE: The range is 6 km at a visibility of 5 km.

Commenting on all three of the aerosols, it is apparent that the effects of mid-IR scattering are very significant for wavelengths shortward of 5.0 μm for all visibilities. Even for wavelengths of 5.0 μm, the scattering is significant for the fog and desert aerosols at visibilities less than 7 km. There are a few cases in the 3.0–3.2 μm and the 4.2–4.8 μm wavelength bands where the scattering fraction is relatively low at higher meteorological visibilities, but, again, these correspond to regions that also have relatively low mid-IR transmission due to line and continuum absorption. An examination of figures 25–33 also shows a progressive movement towards increased scattering for each aerosol type with lower visibilities. Due to its smaller particle size relative to mid-IR wavelengths, the urban aerosol shows considerably less scattering, with relatively insignificant scattering for visibilities down to about 5 km for the MLS atmosphere.

One phenomenon that is plainly seen for the advection fog aerosol in the MLS atmosphere at 3.0 and 4.0 μm is an apparent "reversal" of the slope of the scattering fraction with respect to visibility at low visibilities (refer to figure 25, 4.0 μm in particular). At visibilities below about 8 km, the scattering fraction actually declines with decreasing visibility. The desert and urban aerosols show much weaker evidence of this trend, if they do at all, and at lower visibility thresholds. The cause of the slope reversal can be explained by examination of figure 34. In that figure we have plotted the various components of equation 4 at a wavelength of 4.0 μm. At high visibilities/low optical depths (the optical depth scale at the bottom of the plot corresponds to the symbols on the SS curve) the number density of the particles is low. In cases such as this, single scattering predominates, i.e., the particles are spaced so far apart that usually only one scattering occurs between the source and observer; in that event, the scattering fraction increases as the LOS optical depth increases. However, the solar irradiance available for scattering into the LOS begins to diminish as the optical depth of the hazy boundary layer increases beyond a certain point due to two mechanisms. The first of these is removal of direct beam irradiance by absorption and diffuse multiple scattering within atmospheric layers above the LOS. The second mechanism lies in the nature of the diffuse multiple scattering itself: a considerable fraction of the incident solar radiation is "reflected" back to space, is lost to the ground plane, or stays within the boundary layer but never reaches the LOS region. Thus, as the number density increases, thereby decreasing the visibility, scattering into the LOS gradually increases until the particles reach such a density that the scattering becomes more isotropic and less radiation is scattered into the LOS.

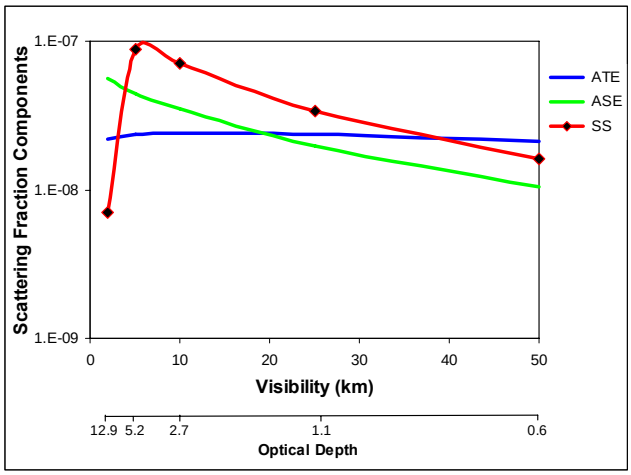

Figure 34. The scattering fraction components for the heavy advection fog at 4.0 µm. The MLS atmospheric profile was employed.

Examination of figures 25–33 shows another interesting phenomenon: the order of the scattering fraction is reversed for the MLS atmosphere for all aerosol types relative to the MLW and SAW atmospheres. For the MLW and SAW atmospheres, the 4.0 µm scattering fraction lies between the 3.0 and 5.0 µm curves. While this is apparent in the visibility curves, a careful examination of the ATE, ASE, and SS curves as a function of model atmosphere (e.g., figures 5 and 6, 8 and 9, and those of the fog aerosol (not presented)), shows that, while significant differences exist for the ATE and ASE scattering fraction components (the SS component has the smallest variation), they do not explain the apparent inversion of the 3.0 and 4.0µm curves in figures 25, 28, and 31, relative to the curves in figures 26 and 27, 29 and 30, and 32 and 33, respectively, and therefore is not a function of visibility. Since we can find no effects due to changes in the aerosols, we conclude that this is purely an effect of the Earth's atmosphere. To verify this, clear-air MODTRAN runs were made for a vertical path from the surface to 100 km using the MLS and MLW atmospheres, the former having a higher absolute humidity profile. As suspected, and presented in table 4, there is significantly decreased transmission at 3.0 µm relative to 4.0 µm between the two model atmospheres employed. This decrease in transmission at 3.0 µm, and also at 5.0 µm, relative to the 4.0 µm transmission, is due to increased line absorption by water vapor.

Table 4. Clear-air transmission from surface level to 100 km along a vertical path using the MLS and MLW atmospheres.

Wavelength (µm)	Transmission	
	MLS Atmosphere	MLW Atmosphere
3.0	0.23	0.71
4.0	0.87	0.87
5.0	0.12	0.52

3.5 Equivalent Blackbody Temperature

Figures 35 and 36 present the equivalent blackbody temperature (EBBT) for the MLS and SAW atmospheres and the urban and desert aerosols: note the difference in temperature scale between the two figures. Determination of the EBBT includes all atmospheric effects considered in this study, as presented in figure 2. Again, it is no surprise that the EBBT is significantly higher for the MLS atmosphere as compared to the SAW atmosphere. We also see the same type of behavior as we have seen before when comparing the EBBT for the urban versus the desert aerosol: the urban aerosol's significantly lower albedo and higher absorption coefficient yields higher emission.

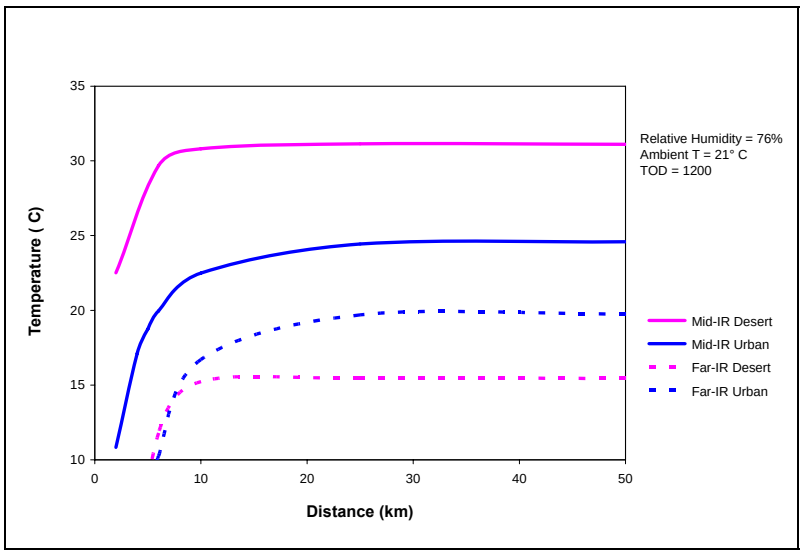

Figures 35. Equivalent blackbody temperature for the urban and desert aerosols with a visibility of 5 km as a function of range, in mid- and far-IR wavelength bands for the MLS atmospheric profile with an ambient temperature of 21 °C.

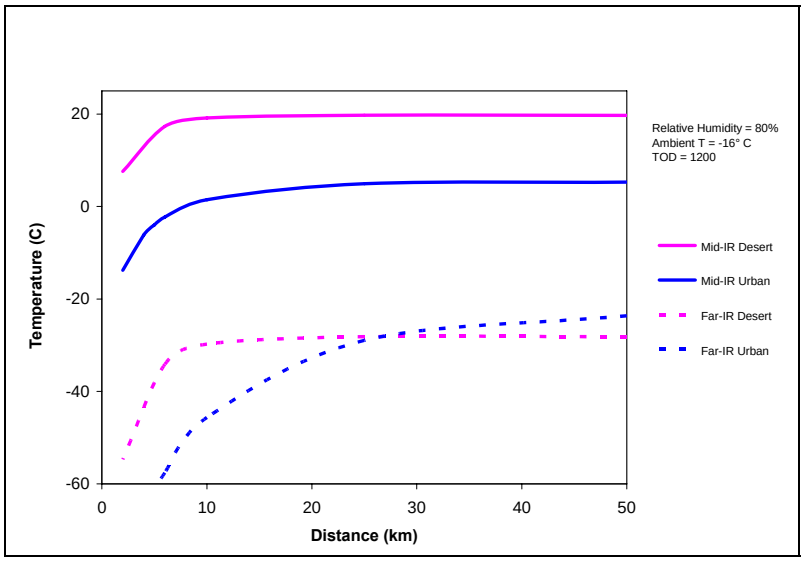

Figure 36. Equivalent blackbody temperature for the urban and desert aerosols with a visibility of 5 km as a function of range, in mid- and far-IR wavelength bands for the SAW atmospheric profile with an ambient temperature of -16 °C.

Examination of both figures does show the effect of "limiting path radiance." Limiting path radiance is the point at which, no matter how large the range becomes, the EBBT remains constant. This effect can be thought of as the point where transmittance goes to zero and the path radiance, from atmospheric in-scattering and thermal emission, becomes constant.

3.6 Instrument Response Function Effects

To examine the impact of aerosol scattering on broadband sensors operating in the mid-IR we filtered the target contrast through Gaussian instrument response functions. We selected the MLS and SAW model atmospheres and the desert and urban aerosol models to represent background temperature and scattering albedo extremes. In order to maximize scattering impacts, we used our basic scenario: a meteorological visibility of 5 km with a horizontal LOS of 6 km. MODTRAN was run at maximum spectral resolution (1 cm^{-1}) in the 3–5 μm band and with the two-stream multiple scattering option active. Using the values from table 2, the thermally emissive target is non-reflective (black), and 1.5 K warmer than the atmosphere that surrounds it.

The sensor performance metric that we used is the apparent target contrast $C(s)$ against the background atmosphere for a sensor-target separation s:

$$C(s) = \frac{L_t(s) - L_b(s)}{L_b(s)}, \tag{5}$$

where $L_t(s)$ is the apparent target radiance and $L_b(s)$ is the apparent background radiance. Both of these quantities are weighted by the instrument response function and integrated over the bandpass where the sensor response is significant.

We applied the following instrument response functions: uniform, i.e., rectangular over the 3.0–5.0 μm band, and three Gaussians. The first Gaussian spanned from 3.0 - 4.2 μm, the second from 4.4 - 5.0 μm, and a third was bimodal, which was a composite of the first two. These instrument response functions, $S_i(\lambda)$, were used to obtain the associated apparent contrasts

$$C_i = C_U,\ C_L,\ C_H, \text{ or } C_B, \tag{6}$$

where U refers to the uniform, or rectangular function, L and H refer to the first, or low (3.0–4.2 μm), and second, or high (4.4–5.0 μm), bands, respectively, and B refers to the bimodal combination. The center positions and widths of the Gaussian functions were selected by examination of both apparent ΔT's curves for the desert and urban aerosols using the MLS and SAW model atmospheres (figures 11, 13, 14, and 16). These graphs are reproduced here with the spectral instrument response functions, $S_L(\lambda)$, $S_H(\lambda)$, and $S_B(\lambda)$, superimposed, and presented as figures 37–40. Recall that the magenta line is transmission only and the blue line includes all scattering and emission effects. Note that, in figures 37–40, the ΔT curve determined by considering transmission + scattering has a separate right-hand scale. The "transmission optimized" low and high band instrument response curves were chosen to maximize sensor response at those wavelengths where apparent target ΔT was highest for the case where only transmission was considered, i.e., the magenta curves. The "scattering optimized" response curves were chosen for the case where both scattering and transmission effects upon the target signature were considered, i.e., the blue curves. The low and high Gaussian instrument response functions selected for the "transmission optimized" case were

$$S_{L,H} = e^{-\pi\left(\frac{\lambda-\lambda_{L,H}}{\sigma_{L,H}}\right)^2};\ \lambda_{L,H} = \{3.75, 4.65\}; \sigma_{L,H} = \{0.371, 0.212\}, \tag{7}$$

where $\lambda_{L,H}$ are the low and high band peak positions and $\sigma_{L,H}$ are the low and high band Gaussian widths, in micrometers. The corresponding response functions for the "scattering optimized" case are given by

$$S_{L,H} = e^{-\pi\left(\frac{\lambda-\lambda_{L,H}}{\sigma_{L,H}}\right)^2};\ \lambda_{L,H} = \{4.0, 4.7\}: \sigma_{L,H} = \{0.159, 0.106\}. \tag{8}$$

The target contrast is then computed from the weighted spectral integration over the interval Δλ by

$$C_i = \frac{\int_{\Delta\lambda} S_i(\lambda)\, L_t(s,\lambda)\, d\lambda - \int_{\Delta\lambda} S_i(\lambda)\, L_b(s,\lambda)\, d\lambda}{\int_{\Delta\lambda} S_i(\lambda)\, L_b(s,\lambda)\, d\lambda}, \tag{9}$$

where i represents either the U, L, H, or B instrument response functions.

Note that the choice of instrument response function shape and position is only approximate. Non-Gaussian functional forms that closely mirror the actual apparent ΔT versus wavelength curves could have been used, but that choice would not affect the qualitative conclusions and would not be very realistic, as real instrument response curves are difficult to modify to arbitrary spectral curves.

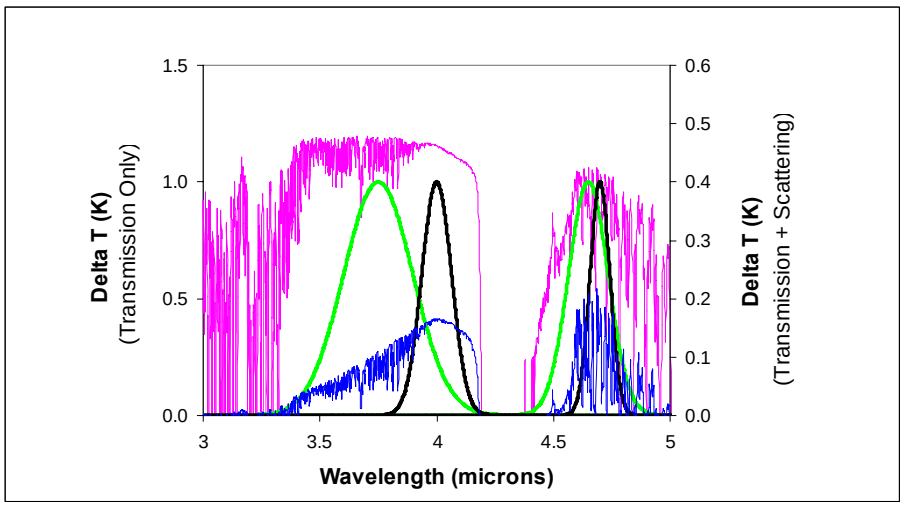

Figure 37. Apparent target thermal contrast for the desert aerosol employing the MLS atmosphere, with transmission optimized (green) and scattering optimized (black) instrument response functions.

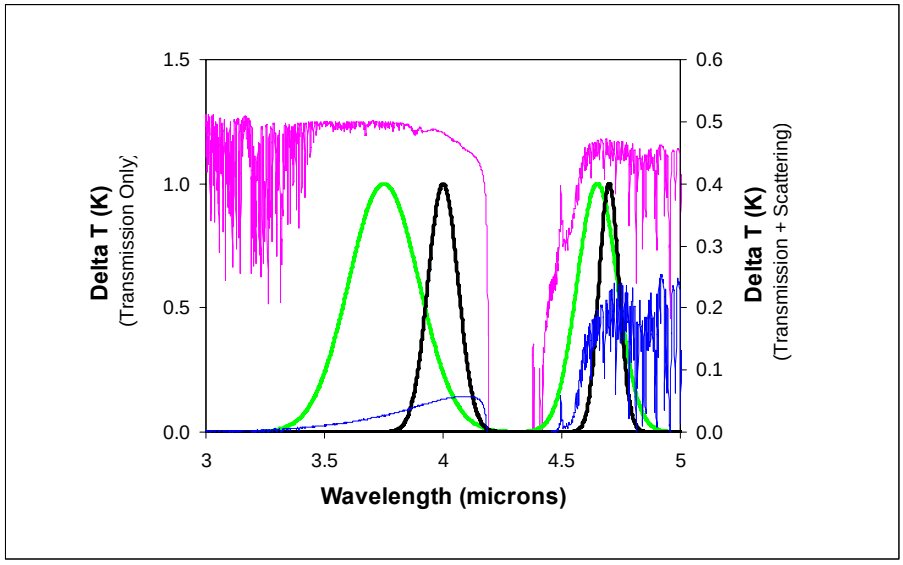

Figure 38. Apparent target thermal contrast for the desert aerosol employing the SAW atmosphere, with transmission optimized (green) and scattering optimized (black) instrument response functions.

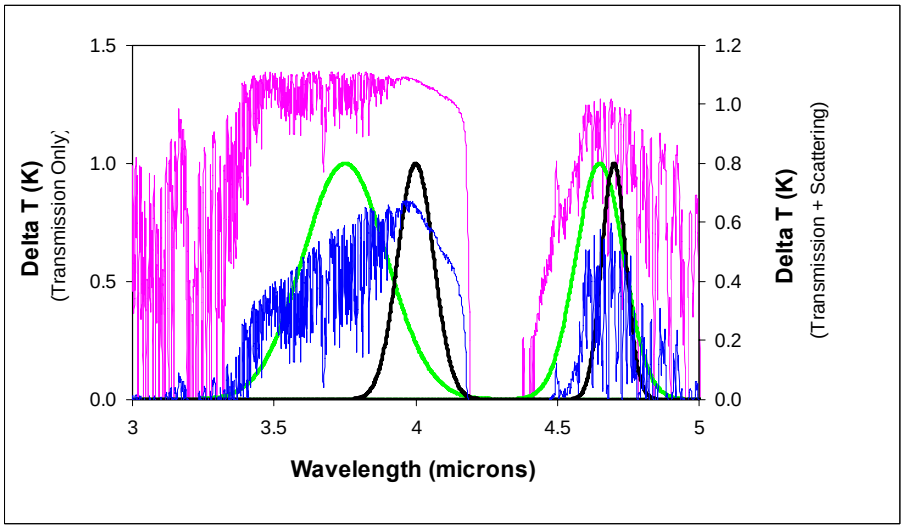

Figure 39. Apparent target thermal contrast for the urban aerosol employing the MLS atmosphere, with transmission optimized (green) and scattering optimized (black) instrument response functions.

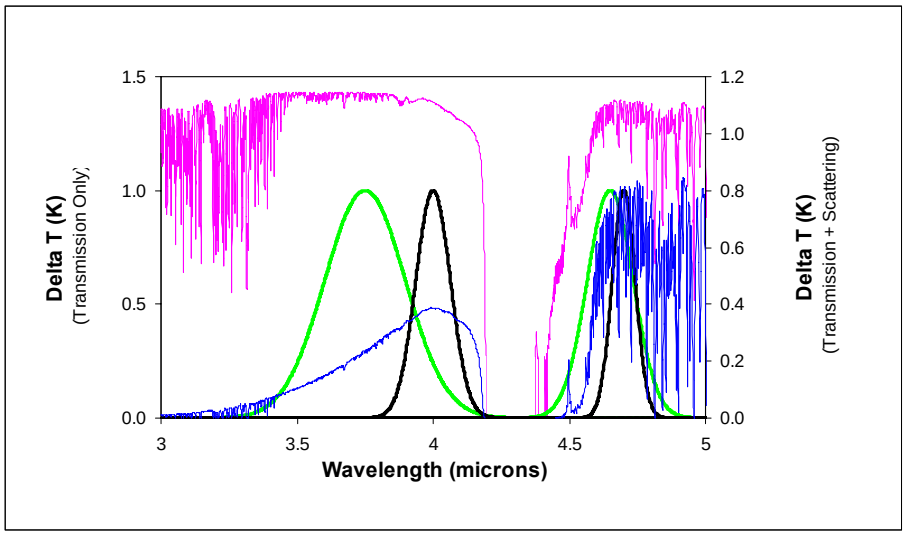

Figure 40. Apparent target thermal contrast for the urban aerosol employing the SAW atmosphere, with transmission optimized (green) and scattering optimized (black) instrument response functions.

The apparent contrasts for the chosen aerosols and atmospheric profiles for the different optimizations and instrument response functions are presented in tables 5–8. Note that, in general, the contrasts are very low due to the small value of ΔT and the zero target albedo. Also note that L_t, the uniform response, band-integrated apparent target radiance, is smaller for the urban aerosol than the desert aerosol in a given background atmosphere. This is primarily due to the larger scattering coefficient for the larger, higher albedo desert aerosol particles. For a given aerosol, L_t is larger for the warmer MLS atmosphere, due to the increased thermal emission radiance from both the target and atmosphere.

Table 5. Apparent target contrast for desert aerosol employing the MLS atmosphere using different optimizations and instrument response functions.

MLS, Desert Aerosol, C_U =0.00206, L_t =1.85 W m^{-2} ster^{-1}			
Optimization	C_L	C_H	C_B
Transmission	0.003666	0.002791	0.003232
Scattering	0.00599	0.003282	0.004551

Table 6. Apparent target contrast for desert aerosol employing the SAW atmosphere using different optimizations and instrument response functions.

SAW, Desert Aerosol, C_U =0.00203, L_t =1.04 W m^{-2} $ster^{-1}$			
Optimization	C_L	C_H	C_B
Transmission	0.001062	0.006567	0.00238
Scattering	0.002127	0.008037	0.004187

Table 7. Apparent target contrast for urban aerosol employing the MLS atmosphere using different optimizations and instrument response functions.

MLS, Urban Aerosol, C_U =0.00719, L_t =1.59 W m^{-2} $ster^{-1}$			
Optimization	C_L	C_H	C_B
Transmission	0.0199	0.00801	0.0122
Scattering	0.0247	0.00935	0.0151

Table 8. Apparent target contrast for urban aerosol employing the SAW atmosphere using different optimizations and instrument response functions.

SAW, Urban Aerosol, C_U =0.0136, L_t =0.476 W m^{-2} $ster^{-1}$			
Optimization	C_L	C_H	C_B
Transmission	0.0112	0.0239	0.0173
Scattering	0.0180	0.0294	0.0244

For the MLS atmosphere and both aerosols, it is apparent that $C_L > C_H$, but $C_L < C_H$ for the SAW aerosols. This is because the background thermal radiance is less for the cooler SAW atmosphere, which enhances the contrast of the warmer target. Also, note that C_L improves considerably under the scattering optimization in all cases, whereas the improvements are more modest for the C_H case. This is of course due to the enhanced influence of scattering in the low band.

The results show that the bimodal instrument response function consistently provides higher target contrasts C_B than the uniform response function's C_U. This is because the strong spectral absorption feature located between 4.2 and 4.4 μm is excluded in the former case and not in the latter. This feature adds considerable noise to the overall sensed radiance signal, so any sensor response function that blocks that noise signal will improve performance.

4. Discussion and Conclusions

While it is true that scattering in the 3.0–4.0 μm band is low under some conditions and at some wavelengths, the atmosphere usually has high molecular absorption (and low transmission) in these situations. Line and continuum absorption spectral structure is also highly variable in this region, making blanket statements about the relative importance of emission and scattering essentially impossible. It is sufficient to say that scattering contributions to the path radiance cannot be ignored in the 3.0–4.0 μm region. However, scattering in the 4.4–5.0 μm pass band can sometimes be ignored for normal background aerosols (such as the urban aerosol) in warmer atmospheres.

Thus any mid-IR algorithms used in near-surface target acquisition models should include the effects of aerosol scattering and atmospheric thermal emission. Further, the beginning portion of the mid-IR band (~3.0–4.2 μm), the "notch" region (~4.2–4.4 μm), and the latter portion of mid-IR band (~4.4–5.0 μm), where scattering effects are minimal, should be considered separately.

In general, for this study, we can make the following observations:

1) Within aerosol type, background temperature is the predominant driver for the determination of scattering amount—the higher the temperature, the less scattering is a factor.

2) At higher temperatures, aerosol type can make a significant difference—higher aerosol albedo will result in greater scattering.

3) Visibility variations produce considerable variations in scattering—the lower the visibility, the greater the scattering.

4) There is a substantial difference in contrast values when scattering is considered.

5) There is a significant improvement in sensor performance by excluding strong molecular absorption and aerosol scattering wavelength regions through appropriate choices of instrument response functions.

References

1. Biberman, L.M. "Weather, Season, Geography, and Imaging System Performance," Chapter 29, *Electro-Optical Imaging: System Performance and Modeling*; SPIE Press: Bellingham, WA, 2000.
2. Berk, A.; Bernstein, L.S.; Robertson, D.C. *MODTRAN: A Moderate Resolution Model for LOWTRAN 7*; GLTR-89-0122 [ADA214337]; Geophysics Laboratory, 1989.
3. Shettle E.P.; Fenn, R.W. *Models for the Aerosols of the Lower Atmosphere and the Effects of Humidity Variations on Their Optical Properties*; AFGL-TR-79-0214 [ADA085951]; Air Force Geophysics Laboratory: Hanscom Air Force Base, MA, 1979.
4. Longtin, D.R.; Shettle, E.P.; Hummel, J.R.; Pryce, J.D. *A Wind Dependent Desert Aerosol Model: Radiative Properties*; Air Force Geophysics Laboratory Technical Report, AFGL-TR-88-0112 [ADA201951]; Hanscom Air Force Base, MA, 1988.
5. Shirkey, R.C.; Tofsted, D.H. *High Resolution Electro-Optical Aerosol Phase Function Database, PFNDAT2006*; ARL-TR-3877; U.S. Army Research Laboratory: White Sands Missile Range, NM, August 2006.

Acronyms

ASE	atmospheric scattered emission
ATE	atmospheric thermal emission
EBBT	equivalent blackbody temperature
EO	electro-optical
FLIR	forward-looking infrared
FOV	field of view
IR	infrared
LOS	line of sight
MLS	midlatitude summer
MLW	midlatitude winter
MODTRAN	Moderate Transmission
RH	relative humidity
RT	radiative transfer
SAW	subarctic winter
SS	solar scattered
TOD	time of day
ws	wind speed

Distribution List

Army Research Laboratory 1
Attn: AMSRD-ARL-CI (Dr. Gowens)
Adelphi MD 20783-1197

Army Research Laboratory 1
Attn: AMSRD-ARL-CI (P. Clark)
Adelphi MD 20783-1197

Army Research Laboratory 1
Attn: AMSRD-ARL-CI (Dr. Ingram)
Adelphi MD 20783-1197

Army Research Laboratory 1
Attn: AMSRD-ARL-CI-EE (Dr. Hoock)
WSMR NM 88002-5501

Army Research Laboratory 2
Attn: AMSRD-ARL-CI-EE (Dr. Shirkey)
WSMR NM 88002-5501

Army Research Laboratory 2
Attn: AMSRD-ARL-CI-EE (Dr. O'Brien)
WSMR NM 88002-5501

Army Research Laboratory 1
Attn: AMSRD-ARL-CI-EE (D. Tofsted)
WSMR NM 88002-5501

Army Research Laboratory 1
Attn: AMSRD-ARL-RO-EN (Dr. Bach)
PO Box 12211
Research Triangle Park, NC 27009

Army Materiel Systems Analysis Activity 1
Attn: AMXSY-SC (J. Mazz)
392 Hopkins Road
APG MD 21005-5071

Army Materiel Systems Analysis Activity 1
Attn: AMXSY (R. Kistner)
392 Hopkins Road
APG MD 21005-5071

Army Materiel Systems Analysis Activity 1
ATTN: AMSXY
APG MD 21005-5071

Army Dugway Proving Ground 1
STEDP MT M
Attn: J. Bowers
Dugway UT 84022-5000

USACE Engineer Research & Development Center 1
Cold Regions Research and Engineering Laboratory
Attn: Dr. Koenig
72 Lyme Road, Hanover, New Hampshire, USA
03755-1290

Army Corps of Engineers 1
Topographic Engineering Center
Data and Signature Analysis Branch
Ft. Belvoir, VA 22060

US Army Night Vision & Electronic Sensors
Directorate 1
Attn: AMSRD-CER-NV (R. Driggers)
10221 Burbeck Road
Fort Belvoir, VA 22060-5806

US Army Night Vision & Electronic Sensors
Directorate 1
Performance Model Development Branch
Attn: AMSRD-CER-NV-MS-PMD (J. Hixson)
10221 Burbeck Road
Fort Belvoir, VA 22060-5806

Director, USA TRADOC Analysis Center 1
Attn: ATRC-W (P. Blechinger)
WSMR, NM 88002-5502

Director, USA TRADOC Analysis Center 1
Attn: ATRC-WA (L. Southard)
WSMR, NM 88002-5502

Director, USA TRAC Anal Ctr 1
Attn: ATRC-FM (T. Bailey)
255 Sedgwick Ave
Ft Leavenworth, KS 66027-2345

Director, USA TRAC Anal Ctr 1
Attn: ATRC-FMA (T. Gach)
255 Sedgwick Ave
Fort Leavenworth KS 66027-2345

Director, USA TRAC Anal Ctr 1
Attn: ATRC-FMA (S. Glasgow)
255 Sedgwick Ave
Ft Leavenworth, KS 66027-2345

United States Military Academy 1
Attn: Combat Simulation Laboratory (Dr. P. West)
West Point, NY 10996

Battle Command Simulation and Experimentation Directorate 1
Army Model and Simulation Division
Attn: DA G37 (DAMO-SBM)
400 Army Pentagon
Washington, DC 20310-0450

USA PEO STRI 1
Attn: J. Blake
12350 Research Pkwy
Orlando, FL 32826-3276

USAF A3O/W 1
Attn: Col M. Lockhart
1400 Key Blvd Suite 301
Arlington, VA 22209

HQ USAFA/DFLIB 1
2354 Fairchild Drive, Suite 3A10
USAF Academy, CO 80840-6214

AFMC DOW 1
Wright Patterson AFB OH 45433-5000

HQ AFWA/DNX 1
106 Peacekeeper Dr STE 2N3
Offutt AFB NE 68113-4039

Naval Research Laboratory 1
Attn: Dr. Goroch
Marine Meteorology Division, Code 7543
7 Grace Hopper Ave
Monterey, CA 93943-5006

U.S. Naval War College 1
Attn: War Gaming Department (Code 33)
686 Cushing Road
Newport, Rhode Island 02841-1207

Naval Weapons Surface Ctr 1
Attn: CODE G63
Dahlgren VA 22448-5000

Head, Astronomical Applications Dept 1
U.S. Naval Observatory
Attn: J. Bangert
3450 Massachusetts Ave., NW
Washington, DC 20392-5420

JWARS 1
Attn: C. Burdick
1555 Wilson Boulevard, Suite 619
Arlington, VA 22209

Northrop Grumman Information Technology 1
Attn: Melanie Gouveia
100 Brickstone Square
Andover, MA 01810-5000

Anteon Corp. 1
Attn: Mike Adams
46 Growing Rd
Hudson, NH 03051

SAIC 1
Attn: Mr. Delgado
731 Lakepointe Centre Dr.
O'Fallon, Ill 62269-3064

Northrop Grumman Corporation 1
Attn: R. Smith
E-10A BDT SEIT M&S IPT Lead
MS B06-222
2000 NASA Blvd
Melbourne, Florida 32907

AFRL/IFOIL 1
525 Brooks Rd
Rome NY 13441-4505

Tech Connect 1
AFRL/XPTC
Bldg 16, Rm 107
2275 D Street
WPAFB OH 45433-7226

AFLR Technical Library 1
Attn: Det 1 AFRL/WSC (Library)
2950 Hobson Way Bldg 642 Rm 1300
Wright-Patterson AFB, OH 45433-7765

WSMR Technical Library 1
Attn: STEWS IM IT
WSMR NM 88002

Technical Reports Boulder Laboratories Library 1
Attn: MC 5
325 Broadway
Boulder, CO 80305

National Center for Atmospheric Research 1
Attn: NCAR Library Serials
PO Box 3000
Boulder CO 80307-3000

Ruth H. Hooker Research Library 1
4555 Overlook Ave, SW
Washington, DC 20375

U.S. Army Research Laboratory 1 CDs
Attn: IMNE ALC IMS
Mail & Records Mgmt
Adelphi, MD 20783-1197

Admnstr 1 electronic copy
Defns Techl Info Ctr
Attn: DTIC OCP (V Maddox)
8725 John J Kingman Rd., Ste. 0944
Ft Belvoir, VA 22060-6218

U.S. Army Research Laboratory 2 CDs
Attn: AMSRD ARL CI OK TL Techl Lib
2800 Powder Mill Rd.
Adelphi, MD 20783-1197

U.S. Army Research Laboratory 2 CDs
Attn: AMSRD ARL CI OK TP Techl Lib
APG, MD 21005

Total 52
(46 hard copies & CDs both +
5 CDs only +
1 electronic copy)

INTENTIONALLY LEFT BLANK.